Catalysis Science & Technology

ROYAL SOCIETY OF CHEMISTRY

MINI REVIEW

View Article Online
View Journal | View Issue

Cite this: *Catal. Sci. Technol.*, 2021, **11**, 5712

Copper-alloy catalysts: structural characterization and catalytic synergies†

Shanghong Zeng,*[ab] Shiyao Shan,[b] Aolin Lu,[b] Shan Wang,[b]
Dominic T. Caracciolo,[b] Richard J. Robinson,[b] Guojun Shang,[b] Lei Xue,[a]
Yuansong Zhao,[a] Aiai Zhang,[a] Yang Liu,[a] Shangpeng Liu,[a] Ze Liu,[a] Fenghua Bai,[a]
Jinfang Wu,*[a] Hong Wang[c] and Chuan-Jian Zhong*[b]

Catalysis plays a significant role in most processes of the chemical industry, especially in the emerging areas of sustainable energy and clean environment. A major challenge is the design of catalysts with the desired synergies in terms of activity, selectivity, stability, and cost. New insights into many fundamental questions related to the challenge have sparked a surge of interest in recent years in the area of exploring copper-based alloy catalysts. In this review, the most recent progress in the explorations of copper-alloy catalysts will be highlighted, with a focus on the structural and mechanistic characterizations of the catalysts in different catalytic reactions. The fundamental understanding of the detailed catalytic synergies of the catalysts for the targeted heterogeneous catalytic reactions depends strongly on the utilization of various analytical techniques for the characterization. Significant progress has been made in utilizing advanced techniques, both *ex situ* and *in situ*/*operando* characterizations, demonstrating the abilities to gain atomic/molecular level insights into the morphological, structural, electronic and catalytic properties of copper alloy catalysts, especially the dynamic surface active sites under the reaction conditions or during the catalytic processes. The focus on structural characterization in this review serves as a forum for discussions on structural and mechanistic details, which should provide useful information for identifying challenges and opportunities in future research and development of copper-alloy catalysts.

Received 14th April 2021,
Accepted 25th June 2021

DOI: 10.1039/d1cy00179e

rsc.li/catalysis

1. Introduction

Many of the environmental issues in the 21st century are recognized as major as-yet-unsolved challenges, including air and water quality improvement and ozone layer protection in the coming decades.[1–6] To date, catalysis has played a significant role in addressing some of these challenges, with a focus on sustainable energy and clean environment by development of efficient catalysts.[7] Indeed, there is a clear drive to seek the most active, selective, robust, and low-cost catalysts for targeted catalytic reactions. Various noble and non-noble metals have been widely exploited as catalysts.[8–12] Significant progress has been made in the exploration of earth-abundant copper and copper-containing alloys as heterogeneous catalysts for various reactions relevant to sustainable energy and clean environment.[13–15]

In recent years, intriguing structural and catalytic properties have been discovered for various copper-based nanostructured catalysts, such as nanoparticles (NPs), nanowires (NWs), nanoalloys (NAs), *etc.*,[16–22] which have led to increasing research interest in advancing the design and preparation of nanoscale copper and copper-alloy catalysts for enhancing the catalytic performances. This enhancement depends strongly on the preparation of catalysts by design and the understanding of the catalytic synergies in various reactions, which rely heavily on our abilities to perform *ex situ* and *in situ*/*operando* structural characterizations of the catalysts for the targeted reactions (Fig. 1).[21–25] In the last decade, many advanced analytical techniques have been used for the characterization of copper/copper oxide and copper-alloy catalysts in terms of morphologies, structures, and reaction mechanisms.

While *ex situ* characterization provides useful information for establishing the synthesis methods and screening the

---

[a] *Inner Mongolia Key Laboratory of Chemistry and Physics of Rare Earth Materials, School of Chemistry and Chemical Engineering, Inner Mongolia University, Hohhot, Inner Mongolia 010021, P.R. China. E-mail: zengshanghong@imu.edu.cn*
[b] *Department of Chemistry, State University of New York at Binghamton, Binghamton, NY 13902, USA. E-mail: cjzhong@binghamton.edu*
[c] *School of Chemical Engineering, Inner Mongolia University of Technology, Hohhot, Inner Mongolia, 010051, P.R. China*

† Electronic supplementary information (ESI) available. See DOI: 10.1039/d1cy00179e

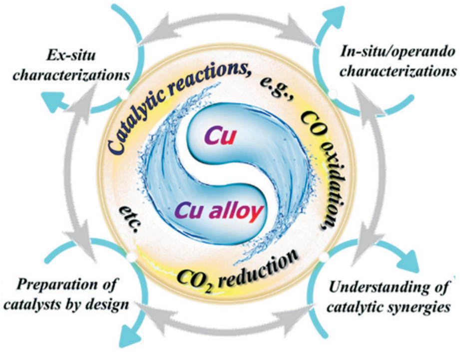

Fig. 1 Illustration of the overall research activities on the preparation, structural characterization and catalytic synergies of Cu and Cu-alloy catalysts for various catalytic reactions.

catalysts in terms of structure changes before and after the catalytic reactions, *in situ*/*operando* characterization provides in-depth and insightful information for assessing the real-time structures and structural changes of the catalysts under the reaction conditions, which are highly dynamic from the catalysis perspective. The understanding of the results from both *ex situ* and *in situ*/*operando* characterizations has been further aided by computational modeling, providing valuable information for the preparation of active, selective and stable copper and copper alloy catalysts by design.[26–30]

Since the progress of research in the synthesis and preparation of different as-synthesized copper-based catalysts has been discussed in several recent reviews,[31,32] readers are referred to those reviews for details on the catalyst preparation aspect. This review focuses on the structural characterization of copper-alloy catalysts, with limited attention to some of the copper alloy preparation methods and the post-synthesis treatments which refine the structures and properties of the as-prepared copper-alloy catalysts. This review will attempt to highlight mainly some of the insights into the catalytic synergies of copper alloy catalysts in selected catalytic reactions. Depending on the specific structures, the synthesis and preparation of the as-synthesized catalysts vary including traditional impregnation and precipitation, hydrothermal, combustion, reduction, hydrolysis, microwave, reverse micelle, and surfactant-encapsulation method. The different preparation methods have significant influences on the structural, morphological and surface properties of the as-prepared catalysts. The catalytic properties of the catalysts can thus be tuned by the synthesis and preparation conditions (see ESI† Table S1).

Gaining an insight into the catalytic synergy or mechanism strongly depends on the abilities to observe the structures, morphologies, phase properties, active sites, and reaction intermediate species on the surfaces and most importantly their changes in catalytic reactions at the atomic and molecular levels.[33–46] As highlighted by selected examples in this review, significant progress has been made in many areas of structural and mechanistic characterizations of the copper alloy catalysts with a number of advanced analytical techniques, which are discussed in terms of *ex situ* and *in situ*/*operando* characterizations separately.

It is important to emphasize that the grouping of the topics of *ex situ* and *in situ*/*operando* characterizations is by no means meant to be exhaustive. Rather, it serves as a forum for discussions on the structural and mechanistic details, which should provide some useful information for identifying the challenges and opportunities in future research and development of catalysts derived from copper alloys.

2. *Ex situ* characterization

The interest in copper-alloy catalysts, especially those with nanoparticle or nanowire structures, is a rapidly emerging area of copper catalysts which have found a wide range of applications in catalytic reactions. The deviation of the nanoalloy structure for copper-alloy nanocatalysts from the structures known for traditional copper or copper oxide catalysts has led to a surge of research interest in the field of heterogenous catalysis in the last decade. An alloy can be broadly defined as a material with mixed metal components with structures ranging from random to ordered mixing or from single phase to phase-segregated states. Alloying copper with other transition metals at the nanoscale leads to intriguing physical and chemical properties that could drastically differ from the monomeric copper or copper oxide counterparts and could produce multifunctional synergies for catalysis or electrocatalysis. As such, the understanding of the copper alloy nanomaterials must involve consideration of these properties and synergies in correlation with the alloy structures, some of which are discussed in this section in terms of *ex situ* characterization. Most notably are the insights into the detailed nanoalloy phase structures and surface atomic arrangements in copper alloy catalysts and their roles in various catalytic reaction mechanisms, which will be discussed in the next section in terms of *in situ*/*operando* characterization.

2.1. Morphologies and composition distributions

For copper alloy nanocatalysts, the ability to control the morphology and the element distributions in the nanomaterials has been demonstrated to be key for tuning and optimizing their catalytic properties. Significant progress has been made in the past decade developing the ability from the synthesis and thermochemical processing perspectives. The progress stems in part from the use of various characterization techniques to determine the morphologies and composition distribution of copper-alloy catalysts, focusing on tailoring and optimizing the functionality of the copper-alloy nanomaterials by controlled chemical synthesis. The nanoalloy morphologies and element distributions of a host of copper-alloy catalysts have been determined by scanning tunneling microscopy (TEM), high-resolution scanning tunneling microscopy (HRTEM), high-angle annular dark-field scanning transmission electron microscopy

(HAADF-STEM), scanning tunneling microscopy (STM), ambient-pressure X-ray photoelectron spectroscopy (AP-XPS), X-ray energy dispersive spectroscopy (EDX), and synchrotron high-energy X-ray diffraction (HE-XRD) coupled with pair distribution function (PDF) analysis.

The catalytic performance of copper-alloy catalysts strongly depends on the size, morphology, structure, distribution, and other intrinsic properties. Copper-alloy catalysts are increasingly attractive in heterogeneous catalysis due to their lower cost, enhanced catalytic performance, high resistance to poisoning and superior stability.[42] To date, copper-alloy catalysts with different morphologies were reported, including nanocrystals, nanocubes, and nanowires. The morphology can be regulated by the change of the critical preparation parameters, aiming to improve the generation of catalytically active sites.[48–51] One example involves the formation of AuCu nanocubes *via* structural evolution in two different pathways: (i) wet chemical reduction of mixed metal precursors and (ii) thermally-activated cross-reactive processing of a binary solution of metal nanoparticles (Fig. 2 middle panel).[52]

While the AuCu alloy nanoparticles formed by pathway-i feature a spherical shape, the AuCu alloy formed by pathway-ii displays a cubic shape (Fig. 2 top panel) which is evidenced by both the lattice fringes and the fast-Fourier transform (FFT) pattern revealing (200) interatomic planes. By supporting the nanoparticles on carbon followed by thermochemical treatment at 260 °C (in 15% O_2) and then at 400 °C (in 15% H_2), the nanoparticles show high crystallinity and a uniform distribution of Au and Cu across the entire nanoparticle, as evidenced by the HAADF-STEM imaging and EDS elemental mapping (Fig. 2 bottom panel). These findings demonstrate the tunability of the shape and the composition for AuCu alloy nanoparticles by thermally-activated interparticle coalescence. This tunability is important for exploring the catalytic synergy of the AuCu catalysts in catalytic reactions (*e.g.*, CO oxidation, to be discussed in a later subsection).

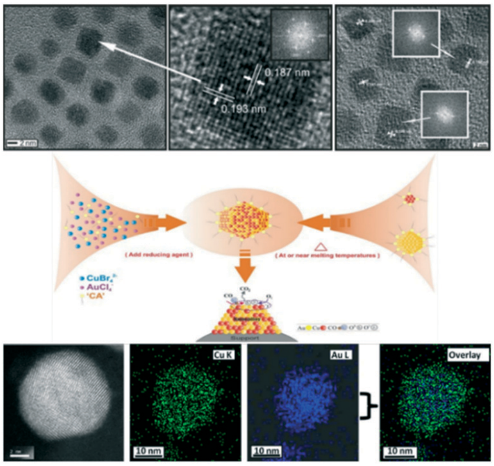

Fig. 2 Top panel: HRTEM image (insert: fast Fourier transform (FFT) pattern) of $Au_{66}Cu_{34}$ alloy nanocubes formed from a binary solution of Cu nanoclusters and Au nanoparticles. Middle panel: Illustration of two different pathways for synthesis and processing of AuCu alloy nanoparticles: wet chemical reduction of the two metal precursors (pathway-i) and cross-reactive evolution of a binary solution of Cu and Au nanoparticles at or near the nanoscale melting temperature (pathway-ii). Bottom panel: HAADF-STEM image and X-ray energy dispersive spectroscopy (EDS) elemental mapping of a single carbon-supported $Au_{40}Cu_{60}$ particle after thermochemical treatment. Reprinted with permission from ref. 52. Copyright 2012 American Chemical Society.

Bimetallic nanostructures have emerged as one important class of active and selective catalysts for gas-phase reactions and CO_2 reduction reaction. The enhancements in the selectivity of CO_2 reduction to multi-carbon hydrocarbons have been observed by tuning the morphologies of bimetallic CuAg catalysts.[53] Hoang *et al.* demonstrated the importance of the morphology of copper–silver alloys for selective electroreduction of CO_2 to ethylene and ethanol.[54] A wire-like morphology of Cu is obtained by electrodeposition of Cu in the presence of 3,5-diamino-1,2,4-triazole (DAT). The CuAg film electrodeposited without DAT displays large particles, whereas the nanoporous CuAg catalyst obtained in the presence of DAT exhibits a wire-like morphology and high porosity. The latter exhibits the best catalytic performance for CO_2 electroreduction to C_2H_4 and C_2H_5OH. The wire-like morphology is associated with the high surface area, homogeneous mixture of Cu and Ag and the stability of the Cu_2O overlayer.

A solid-solution alloy ensures a homogeneous distribution of the constituent elements. The bifunctional effects and the change in the electronic state in solid-solution copper-alloy catalysts were studied on novel Ru–Cu solid-solution alloy nanoparticles, which are immiscible even above the melting point in the bulk phase.[55] The $Ru_{0.5}Cu_{0.5}$ nanoparticles were prepared by the polyol method under a N_2 atmosphere, using ruthenium acetylacetonate $Ru(acac)_3$ as a precursor. The characterization results of $Ru_{0.5}Cu_{0.5}$ solid-solution nanoparticles from high-angle annular dark-field scanning TEM, EDX elemental mapping and synchrotron powder X-ray diffraction show that Ru and Cu are homogeneously distributed in the face-centered cubic (fcc) structure (Fig. 3). The $Ru_{0.5}Cu_{0.5}$ solid-solution catalyst presents excellent CO oxidation activity in comparison with Ru nanoparticles. Here, Ru demonstrates a strong capability for CO adsorption, and Cu has a high chemical affinity for the O atom. The bifunctional effects and the change in the electronic state of Ru contribute to the enhanced catalytic activity for CO oxidation.

One-dimensional nanowires present unique properties. One area of current research interest involves preparing multi-metallic copper-alloy nanowires where synergistic catalytic sites can be created along the surface of nanowires in contrast to nanoparticle catalysts. The composition-dependent catalytic synergy improves the catalytic performance. PtCu nanowires of different compositions for the methanol oxidation reaction were reported by Liao *et al.*, in which the HAADF-STEM imaging and elemental mapping

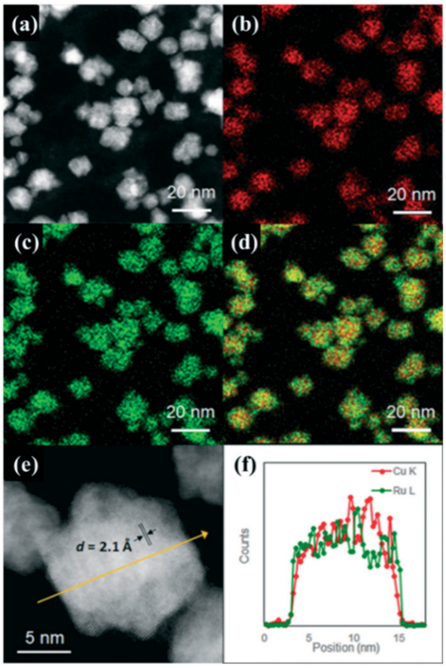

Fig. 3 (a) HAADF image, (b) Cu-K STEM-EDX map, (c) Ru-L STEM-EDX map, (d) reconstructed overlay image of the Cu-K STEM-EDX and Ru-L STEM-EDX maps, (e) HR-STEM image, and (f) compositional line profiles of Cu and Ru for $Ru_{0.5}Cu_{0.5}$. Red, Cu; green, Ru. Reprinted with permission from ref. 55. Copyright 2017 American Chemical Society.

data provided important information for assessing the roles played by the morphology and composition in the catalytic synergy.[56] For example, $Pt_{32}Cu_{68}$ nanowires exhibit ultrathin diameters and a uniform distribution of Pt and Cu along and across the nanowire. The PtCu NWs feature an interconnected network structure of NW bundles, and the distributions of Pt and Cu elements are homogeneous throughout the NW bundles. A close examination of the bundles reveals well-aligned ultrathin NWs. The NWs are highly monodispersed with a narrow diameter distribution (1.3 ± 0.2 nm). The high-resolution TEM image of an individual NW shows the (111) planes of the face-centered-cubic (fcc) alloy. The composition-dependent alloying and faceting properties of the NWs were shown to play a major role in the bifunctional synergy responsible for the enhanced electrocatalytic oxidation of methanol,[56] an important reaction in alcohol fuel cells.

Another example of a multi-metallic alloy nanowire is a novel copper atom-pair catalyst anchored on alloy nanowires. Various Cu and Cu-based catalysts have been developed and employed for transforming CO_2 to CO. It is important to understand the active sites and corresponding catalytic mechanisms for the production of CO from CO_2 reduction. In this respect, a two-adjacent-Cu catalyst involving Cu_1^0–Cu_1^{x+} atom-pair structure anchored on PdTe alloy nanowires was recently reported for electrocatalytic CO_2 reduction.[57] XAFS spectroscopy and theoretical calculations have revealed that the Cu_1^{x+} atom features adsorption of H_2O and the neighboring Cu_1^0 atom is capable of absorbing CO_2 in the critical step of CO_2 reduction, thereby promoting CO_2 activation. This results in a faradaic efficiency of CO over 92% as well as the competing hydrogen evolution reaction is almost completely inhibited.

Remarkably, Cu facets are closely related to the active sites for the CO_2 reduction reaction. Herein Nørskov *et al.* used theoretical calculations to compare the effect of Cu facets including (111), (100), and (211) on the energetics of electrocatalytic CO_2 reduction, proposing that the Cu (211) facet is the most active in yielding CO as well as CH_4.[58,59] By contrast, Wang *et al.* identified that metastable facets including (110) and reconstructed (110) would be likely the active sites on the nanocrystalline Cu nanowire catalysts for the low-overpotential electroreduction of CO_2 to CO.[60] Moreover, Yin *et al.*, who created specific facets in metal nanocrystals by a controlled chemical etching method, also demonstrated that enriched high-energy Cu (110) facets exhibit high activity for CO_2 reduction.[61]

Copper-alloy catalysts with different morphologies were synthesized and characterized for catalytic applications in the field of heterogeneous catalysis. The precursors for preparation usually play an important role in the atomic-level mixture of alloy catalysts.[49,50,62] The evidence of synergy between Cu and one or two other metal elements is obtained by multi-characterization techniques. These new insights can provide valuable information for modifying the catalytic performance to favor the further development of rationally designed copper-alloy catalysts.

2.2. Phase structures

The understanding of the atomic-level chemical structure and phase structure of nanoalloy catalysts is essential for the exploration of their unique catalytic properties in many reactions. Significant progress has been made in recent years to characterize the phase structure and composition distribution for different nanoalloy catalysts due to advanced techniques such as high-energy X-ray diffraction (HE-XRD) coupled with pair distribution function (PDF), which provide detailed information on the phase structures in terms of lattice strains and interatomic coordination or spacing. Regular in-house X-ray diffraction (XRD) has also provided limited information for assessing the alloy structures. A series of copper-alloy catalysts have been studied, focusing on understanding the structure–activity correlation. The determination of atomic arrangement in copper-alloy catalysts and the confirmation of the detailed structural properties are necessary for probing the relationship between the atomic structure and catalytic performance.[63] To date, the phase structure of alloy nanomaterials has received increasing attention in order to understand its role in heterogeneous catalysis.[46,64] The structural effect of copper-alloy catalysts is closely associated with their catalytic behavior and alloy stability. This motivates the exploration for the detailed structure responsible for catalytically active species and the search for phase structure-synergy correlation of copper-alloy catalysts.

The phase structures of copper-alloy catalysts strongly depend on the chemical composition and the thermochemical treatment of the catalysts. This is demonstrated in a study of the copper-alloy catalysts prepared by manipulating the bimetallic composition and the temperature of the thermochemical treatment.[65] $Pd_{75}Cu_{25}$ and $Pd_{21}Cu_{79}$ NPs appear as single-phase nanoalloys of the fcc-type structure occurring with both bulk Pd and Cu. $Pd_{48}Cu_{52}$ NPs appear to be segregated into chemically ordered bcc and disordered fcc-type phases occurring in the bulk state. Pd and Cu atoms in the chemically ordered phase occupy the vertices of two interpenetrating simple cubic lattices, whereas Pd and Cu atoms in the chemically disordered alloy phase occupy the vertices of an fcc-type lattice at random. The correlation between phase structure and catalytic performance is revealed by analyzing the details of atomic arrangement in copper-alloy catalysts.

The phase structure is shown to play an important role in the catalytic activity for CO oxidation in addition to the surface oxygenation of Cu species on the PdCu catalyst. The synergy of bimetallic nanoalloy displays a minimum of light-off temperature, corresponding to a maximum of activity, when the Pd : Cu ratio is close to 50 : 50.[65] The structural and catalytic properties are strongly dependent on the bimetallic composition and the phase structure. The Pd and Cu atoms on different facets are more intermixed in the fcc phase than in the bcc phase, which is partially responsible for the enhanced catalytic activity with the fcc-phase at a Pd : Cu ratio of 50 : 50. Qualitatively, the ensemble effect plays an important role in the enhanced catalytic activity for CO oxidation over the PdCu catalyst with a Pd : Cu ~ 50 : 50 ratio.

The phase structures of copper-alloy catalysts are varied with tunable composition, further influencing the electronic structure and catalytic performance. For example, Au–Cu bimetallic thin films with varied composition were synthesized by the magnetron sputtering co-deposition method.[66] As shown in Fig. 4 top, the alloy catalysts have one dominant characteristic peak, corresponding to the diffraction of the (111) plane in face-centered cubic (FCC) crystal structure. The dominant peak shifts to the high-angle direction with increasing content of Cu. Herein, no characteristic peak of pure Au or Cu appears in XRD patterns, indicating that Au and Cu are not phase separated but alloyed in the samples. Interestingly, with increasing atomic ratio of Au, the center of the d-band gradually deviates from the Fermi level, resulting in the decrease of *CO binding strength (Fig. 4 bottom). The weakened strength improves the catalytic activity for electrochemical CO_2 reduction to CO. The studies indicate that the regulation of phase and electronic structure *via* the variation of Au and Cu composition achieves the purpose of improving the selectivity for electrochemical CO_2 reduction.

The insertion of Cu atoms or ions into the lattice of active components or supports is believed to play an important role in the change of the phase structure which affects the catalytic performance.[67,68] Han and his group[69] studied the role of copper in $CoCu/SiO_2$ catalysts for the synthesis of different alcohols. The main diffraction peaks for $5Co2.5Cu/SiO_2$ (weight fraction) were found to be the same with those of Co/SiO_2, whereas the peaks for CuO were absent in the $5Co2.5Cu/SiO_2$ catalyst. The change of the lattice parameters for $5Co2.5Cu/SiO_2$ was attributed to the insertion of Cu atoms into cobalt oxides. The $5Co2.5Cu/SiO_2$ catalyst displayed a three-fold increase in the selectivity to higher alcohols in comparison with that for the Co catalyst. The enhanced performance is explained by the insertion of Cu in the lattice structure, which weakens the CO/HCO dissociation and prevents the formation of CH_x species. The presence of Cu atoms facilitates the control over the size of Co nanoparticles and impedes the insertion of CH_x species.

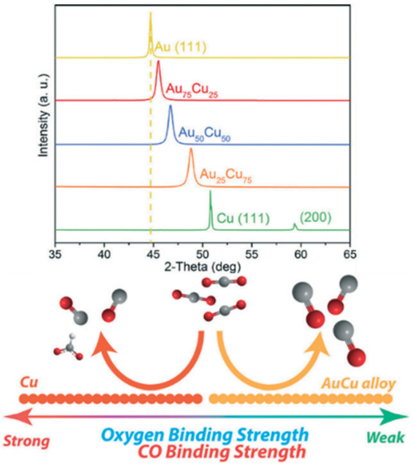

Fig. 4 (Top) XRD patterns of binary metallic AuCu alloy catalysts. (Bottom) Illustration of binding strength on the Cu and AuCu alloy nanoparticles. Reprinted with permission from ref. 66. Copyright 2019 American Chemical Society.

The role of phase structures is investigated on bimetallic copper-alloy catalysts in the oxygen reduction reaction (ORR), providing a fresh understanding of the structure–activity correlation. The structure of Pd and Cu atoms in Pd–Cu alloy NPs shows atomic configurations of very different chemical ordering patterns.[70] This finding demonstrates subtle atomic structure ordering–disordering processes triggered by changes in the bimetallic composition. There is also a significant impact of the thermochemical treatment on the atomic structure of PdCu alloy NPs. The study shows that the phase structures strongly influence the catalytic properties of the catalysts. By different H_2 thermal treatments, the fcc and bcc structures were found to coexist from 200 to 800 °C. Analyses of the atomic PDFs show that the phase states of PdCu/C catalysts strongly depend on the H_2 thermal treatment temperatures (Fig. 5).[70] PdCu/C (H_2/30 °C) and PdCu/C (H_2/100 °C) catalysts feature single-phase alloys with chemically disordered fcc structure. PdCu/C (H_2/200 °C) and PdCu/C (H_2/400 °C) show phase segregation into a mixture of chemically disordered fcc and chemically ordered bcc structures. The analysis reveals 52% fcc and 48% bcc for the PdCu/C (H_2/200 °C) catalyst, showing a fcc-type lattice

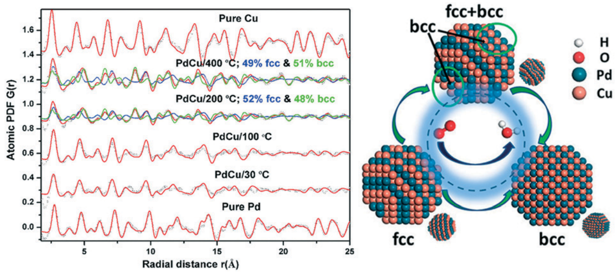

Fig. 5 Experimental (symbols) and crystal structure model-derived (lines) atomic PDFs for PdCu/C after H_2 treatment at different temperatures. Insert on the right: An illustration of the possible phase evolution of the PdCu nanocrystal in terms of fcc and bcc structures and the impact on the catalytic activity for the oxygen reduction reaction. Reprinted with permission from ref. 70. Copyright 2018 American Chemical Society.

parameter of 3.812 Å. The percentage of fcc structure is shown to decrease slightly to 49% when the temperature increases to 400 °C.

This finding demonstrates that the phase structure of the Pd–Cu alloy nanoparticles is highly dependent on the thermal treatment temperature, which has been used as an important pathway for engineering the nanostructures. This study further reveals that the PdCu catalyst with a pure fcc structure has a higher catalytic activity for the oxygen reduction reaction than those featuring a mixture of fcc and bcc phases.

The alloy surface segregation is linked to the stability and catalytic activity of copper-alloy nanoparticles. Many efforts have been made to reveal the structure–property relationship. For example, Zhan *et al.* prepared AuCu alloys with face-centered cubic (fcc) and face-centered tetragonal (fct) structure for catalytic CO oxidation.[71] As shown in Fig. 6a and b, the XRD patterns of the fcc-AuCu and fct-AuCu alloy shifted to the low-angle direction with increasing calcination time, indicating Cu diffusion from the alloy structure on the catalyst surface. The shift is more obvious for fcc-AuCu in contrast with the fct-AuCu alloy (Fig. 6c), and it suggests that Cu diffusion is easier in the former, which is consistent with density functional theory (DFT) calculation. From Cu 2p XPS spectra (Fig. 6d), the oxidation of metallic Cu is confirmed during the calcination. It can be seen from the schematic diagram at the bottom that AuCu alloy nanoparticles are transformed into Au/CuO for fcc-AuCu and AuCu/CuO for the fct-AuCu alloy. Furthermore, more Cu atoms migrate to the surface of fcc-AuCu after the thermal treatment at 250 °C in air compared with the fct-AuCu alloy. The transformation has a direct influence on CO adsorption, and the AuCu/CuO catalyst from the fct-AuCu alloy demonstrates enhanced catalytic activity for CO oxidation, which is attributed to the fine-tuning of crystal structure in the AuCu alloy.

Significantly, the transformation of phase structure from a disordered alloy to an ordered intermetallic structure offers a possibility for precisely tuning the position of atoms in copper-alloy catalysts, aiming to improve the catalytic performance of alloy nanoparticles. For example, Yang *et al.* showed that the atomic ordering transformation could enhance the electrocatalytic selectivity and activity of AuCu alloy nanoparticles for CO_2 reduction.[72] Specifically, it can be seen from Fig. 7a that the AuCu alloy nanoparticles experienced the disorder-to order transformation.

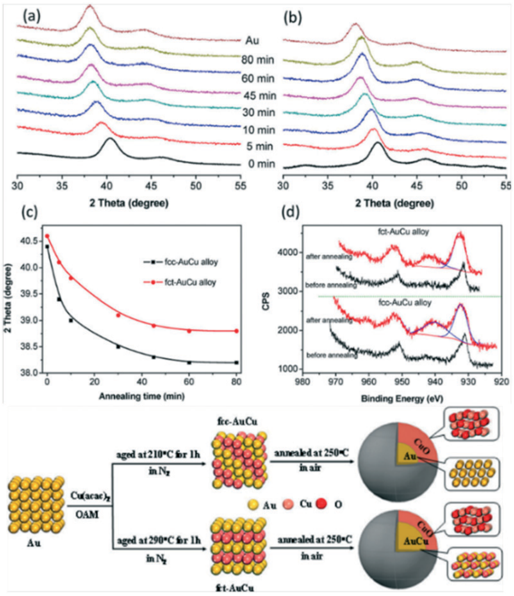

Fig. 6 XRD patterns of (a) fcc-AuCu alloy NPs and (b) fct-AuCu alloy NPs annealed at 250 °C for different times. (c) Corresponding 2 theta for the (111) reflection peak of as-synthesized AuCu alloy NPs with different annealing times. (d) Cu 2p XPS spectra of fcc-AuCu and fct-AuCu alloy NPs. (Bottom) Synthesis illustration of the AuCu alloy NPs and structure transformation annealed at 250 °C. Reprinted with permission from ref. 71. Copyright 2017 American Chemical Society.

XRD measurements (Fig. 7b) show that the crystal structure transitions from face-centered cubic to face-centered tetragonal. The faradaic efficiency of CO exhibits a continuous increase with the ordering degree of AuCu nanoparticles in the sequence from disordered AuCu (d-AuCu), the first intermediate ordered AuCu (i1-AuCu), the second ordered AuCu (i2-AuCu) and the most ordered AuCu (o-AuCu). The o-AuCu nanoalloy selectively catalyzes CO_2 to CO with almost 80% faradaic efficiency, while the d-AuCu nanoalloy favors hydrogen evolution.[72] Gong *et al.* further increased the CO faradaic efficiency to 90.2% by constructing Cu vacancies over the ordered AuCu catalysts, leading to enhanced *COOH intermediate absorption.[39] These findings indicate that regulating phase transformation from disordered to ordered structure in alloy nanoparticles can provide a means for tuning atomic precision and improving the catalytic performance over copper-alloy catalysts.

The tunability of atomic arrangements is known to induce changes in physical and chemical properties responsible for catalytically active sites of copper-alloy catalysts.[73,74] Extensive experimental studies have been made to prepare well-defined copper-alloy catalysts and determine the

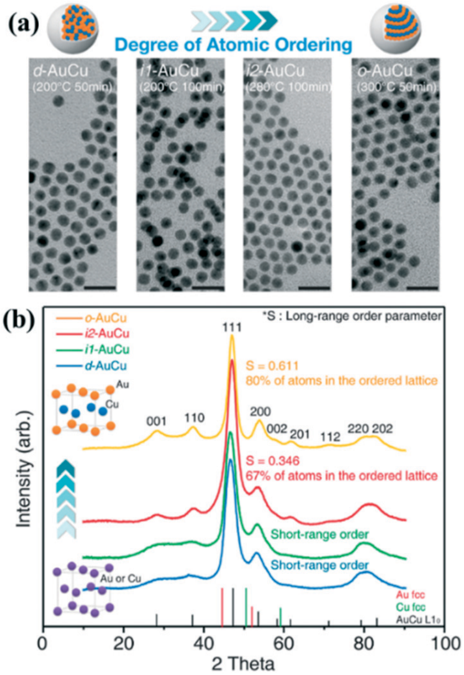

Fig. 7 Atomic ordering transformation of AuCu alloy nanoparticles. (a) TEM images of the AuCu alloy catalysts prepared under different conditions allowing for systematic tuning of the degree of ordering. (b) XRD of the AuCu alloy nanoparticles. Reprinted with permission from ref. 72. Copyright 2017 American Chemical Society.

composition–property relationship. The influence of phase structure on the catalytic performance is also substantiated by theoretical calculations which could bring a significant breakthrough in designing new and efficient copper-alloy catalysts.

2.3. Surface active sites and computational modeling

One of the main aims of contemporary catalytic science is to determine the fundamental origin of the catalytic reaction, which is often done by developing models of catalytic processes at the molecular level. This aim relies on the detailed understanding of the critical role of active sites in the reaction mechanism (*e.g.*, reaction pathway and rate-determining step). High-resolution photoemission spectroscopy (HR-PES) and XPS are powerful tools for characterizing the molecular basis of catalysis. The understanding of the results is also aided by DFT computational modeling in terms of reaction energies and barriers. The recent findings have demonstrated that the active sites of nanoalloys can be rationally tuned by controlling the composition, morphology, and interfacial structure.

Understanding of the detailed surface chemistry on a catalyst is critical for the design of the catalyst of heterogeneous catalysis because the catalytic reaction occurs on the surface of the catalyst.[75–78] HR-PES or XPS characterization is usually used to determine the surface chemistry including the composition, and chemical and electronic states. In addition, first-principles DFT calculations can be applied to predict and study the active species on the surface, the correlation of the catalytic performance with the chemical composition and phase structures.[79] Simultaneously, it also can be used to substantiate the conclusions from experimental studies. When Cu is alloyed with other metal elements, the adsorption energies, the energy barrier of the reaction and the exchange–correlation interaction may change, which can further improve or suppress the process of heterogeneous reactions. The combination of experimental and theoretical studies helps elucidate the real active surface and reaction mechanism.

An XPS study was performed to investigate the electronic state of Au–Cu alloy surfaces. Au is loaded on the surface of the Cu substrate to form an alloy on the surface in order to reduce the amount of gold used and to improve the catalytic performance. For example, Kim *et al.*[80] reported a study of a Au thin layer on a Cu polycrystalline surface for electrochemical reduction of CO_2 to CO. The Au $4f_{7/2}$ peak at 84.0 eV is assigned to polycrystalline Au. For the Au/Cu catalyst, the Au $4f_{7/2}$ peak shifts to a higher binding energy at 84.2 eV, suggesting the presence of charge overcompensation due to the decrease of sd-hybridization. In this work, constructing a thin layer of Au on polycrystalline Cu results in higher adsorption strength between the catalysts and reaction intermediates, further improving the catalytic activity and selectivity for the reduction of CO_2 to CO, which is due to the s-band electron transformation from Cu to Au and the upshift of the d-band center of Au.[80] This shows a promising idea and method for optimizing the copper-alloy catalysts.

The combination of XPS characterization and DFT calculation has been utilized to study the active interface of Cu and In as well as the reaction pathways. When the composition, morphology, and/or interface are rationally tuned, the CuIn compound catalysts show completely different product formation trends or reaction pathways. For example, Zangari *et al.* found that the selectivity of CO_2 reduction depends on the In content of CuIn catalysts as they investigated the dendritic CuIn alloy with various compositions.[81] Specifically, CO production increased with lowering In content, while HCOOH production followed the

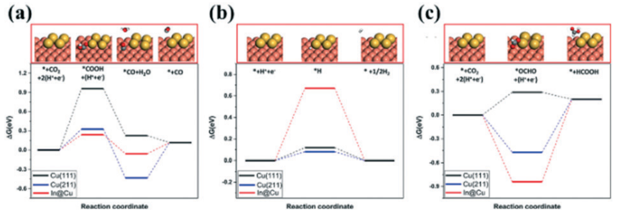

Fig. 8 Free-energy diagrams for (a) CO_2 to CO, (b) H_2 evolution, and (c) CO_2 to HCOOH on Cu(111), Cu(211), and In@Cu surfaces at 0 V *vs.* RHE. The upper panels show the DFT-optimized geometries for each reaction step on In@Cu. Reprinted with permission from ref. 82. Copyright 2018 American Chemical Society.

opposite trend, which is related to the adsorption strength of the key reaction intermediates of CO_2 to CO or HCOOH over the CuIn surface. Meanwhile, Züttel *et al.*[82] reported a facile method to prepare CuIn alloys, including deposition, oxidation and *in situ* electroreduction process. XPS confirmed the formation of a CuIn interface after the above procedures. DFT calculations substantiate the conclusion that the interface of Cu and In plays a fundamental role in controlling the selectivity and reaction pathway of CO_2 reduction. Explicitly compared with Cu (111) and Cu (211) facets, the CuIn interface could decrease the free energy barrier for the *COOH intermediate of CO production (Fig. 8a). It suppresses the activity of competitive H_2 and HCOOH production reactions through the weak and strong adsorption of *H and *OCHO intermediates, respectively (Fig. 8b and c). A similar example is also found for the CuAg catalyst, which displays an enhanced selectivity for CO production compared to pure Cu, suggesting the synergistic effect of Cu-based alloy components.[40]

Theoretical calculations have played an important role in understanding the experimental data which help identify the optimal compositions and origin of enhanced activities for copper-alloy catalysts for different reactions. For example, the study of Cu-alloy catalysts for CO oxidation reveals superior catalytic performance for the nanoalloy with a Pd : Cu ratio close to 50 : 50.[83] The activation of both CO and O_2 is considered important for the understanding of the catalytic synergy of Cu-alloy catalysts in CO oxidation. The origin of the enhanced activity for CO oxidation and oxygen reduction reaction over PdCu nanoalloy catalysts was studied by theoretical modeling (Fig. 9a).[83] With different configurations of Pd_{55}, $Pd_{43}Cu_{12}$, $Pd_{27}Cu_{28}$, $Pd_{12}Cu_{43}$, and Cu_{55} clusters (Fig. 9a), the adsorption sites and modes of CO and O_2 are modeled. As shown in Fig. 9b, the theoretical and experimental results show that the highest catalytic activity of CO oxidation over the $Pd_{50}Cu_{50}$ catalyst is attributed to the weakest adsorption strength of O_2 and the smallest barrier energy for CO oxidation. This finding is consistent with the most pronounced charge transfer between Pd and Cu for CO oxidation over the $Pd_{50}Cu_{50}$ catalyst.

DFT calculations are performed to access the active sites of copper-alloy catalysts with a combination of noble metals and Cu on the surface. For example, the correlation of O_2 activation with the phase structure of fcc and bcc-structured PdCu alloys has been studied in the ORR.[70] Fig. 9c shows the phase evolution of fcc and bcc structures for the PdCu nanoalloy. The O_2 adsorption energy on the fcc-structured surface is greater than that on bcc-structured PdCu(100) alloys (Fig. 9c). A lower reaction barrier and higher reaction energy are displayed on the fcc-structured surface, indicating that the fcc-structured PdCu(100) surface exhibits a higher activity for the O–O cleavage reaction than the bcc-structured PdCu(100) surface. The O–O bond distance (1.453 Å) on the fcc-structured surface is longer than that on the bcc-structured surface (1.405 Å). The fcc-structured (100) surface extends the O–O bond and is expected to facilitate the occurrence of an O–O cleavage reaction. The DFT calculation results reveal a sharp difference and a clear correlation in mass activity between fcc and bcc structures of the PdCu nanoalloys, demonstrating the impact of phase structure on the catalytic properties.

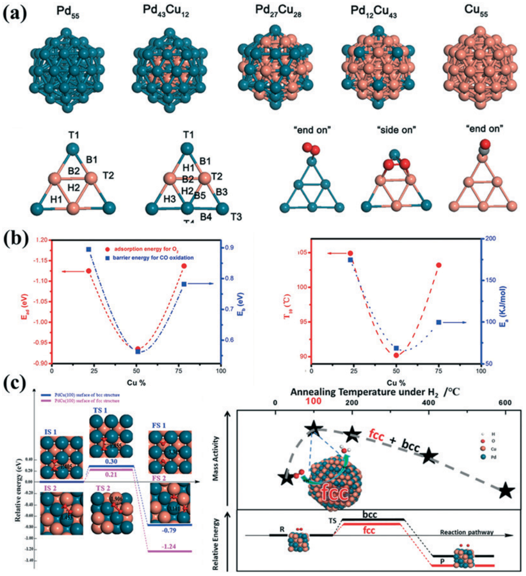

Fig. 9 (a) Models of the metal and alloy nanoclusters, adsorption sites and modes (from left to right): $Pd_{12}Cu_{43}$, and $Pd_{27}Cu_{28}$, O_2 with "end-on", O_2 with "side-on", and CO with "end-on" configurations. (b) (from left to right): Plots of adsorption energy of O_2 and barrier energy of CO oxidation *vs.* Cu %, and T_{10} values (CO oxidation light-off temperature) and E_a *vs.* Cu % for CO oxidation over PdCu/C catalysts. Reprinted with permission from ref. 83. Copyright 2017 American Chemical Society. (c) Energetics of the O–O bond cleavages of the O_2 molecule on the PdCu(100) surface of bcc and fcc crystal structures (left) and correlation between the calculated energy barriers and ORR mass activities (right). Reprinted with permission from ref. 70. Copyright 2018 American Chemical Society.

XPS and XRD, aided with DFT calculations, were applied to probe the active Cu surfaces on copper-alloy catalysts, gaining valuable insights into the nature of active sites. Most recently, the combination of In or Sn with Cu has been considered as a promising catalyst for converting CO_2 to CO.[84–87] For instance, Takanabe *et al.* developed CuIn alloy surfaces for electrochemical reduction of CO_2, and showed about 90% CO faradaic efficiency at 0.6–0.8 V *versus* RHE.[88,89] The XRD pattern of the as-synthesized sample proves the generation of the CuIn alloy. XPS spectra indicate the presence of Cu^0 and In^0 metallic states on the surface. They also revealed, by theoretical calculations as shown in Fig. 10, that In atoms prefer to replace less densely packed Cu atoms and locate on the edge sites.[88] Moreover, In atoms hinder the adsorption of H and CO, but alter the adsorption properties of neighboring Cu atoms. This kind of preference for site occupation and altered adsorption of In atoms could contribute to improving the selectivity for CO over Cu atoms, which shows the total current density (j_{tot}) and faradaic efficiency of CO_2 reduction over oxide-derived Cu (OD-Cu) and CuIn (Cu–In) catalysts from −0.3 to −0.7 V (*vs.* RHE) in

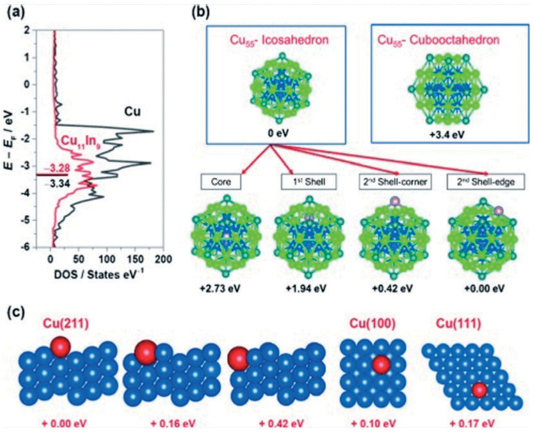

Fig. 10 (a) Density of states of Cu and of $Cu_{11}In_9$. (b) Site preference of In replacing one Cu in the Cu_{55} (Ih) cluster. (c) Side views of the three possible geometries of the (211) facet and top views of (100) and (111) facets of Cu with one In atom replacing a Cu atom. Reprinted with permission from ref. 88. Copyright 2015 Wiley-VCH Verlag GmbH & Co. KGaA, Weinheim.

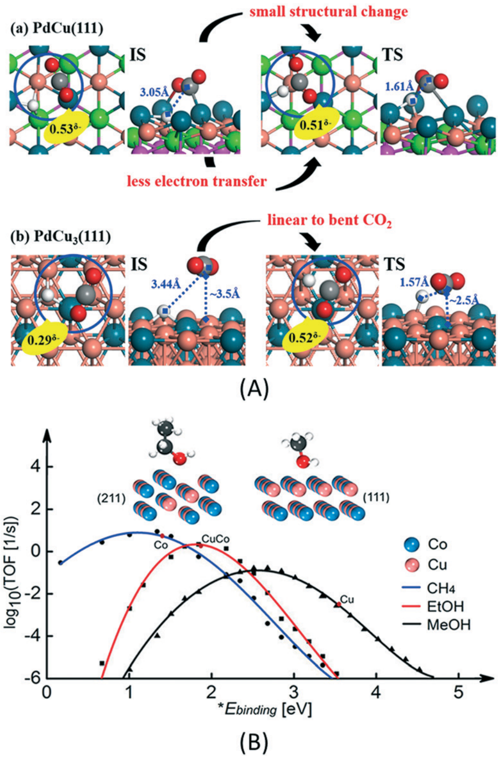

Fig. 11 (A) (a and b) Structural and charge properties of the initial and transition states associated with HCOO* formation. Reprinted with permission from ref. 93. Copyright 2018 American Chemical Society. (B) Plots showing the structure-sensitive selectivity for synthesis gas (CO + H2) conversion over CuCo (211) toward ethanol and (111) toward methanol. Reprinted with permission from ref. 97. Copyright 2018 American Chemical Society.

0.1 M $KHCO_3$ solution. There was a similar total current density, indicating the same electron transfer rates for CO_2 reduction over OD-Cu and CuIn catalysts; however, the presence of In atoms distinctly altered the selectivity. OD-Cu is shown to convert CO_2 to HCOOH and CO at more negatively polarized potential. In contrast, the CuIn catalysts improved the CO selectivity in CO_2 reduction while inhibiting the generation of HCOOH.

The information of Gibbs free energy and binding energy of intermediates from DFT calculations can assist to analyze the active sites and reaction pathway. For example, PdCu alloy nanoparticles have been found to exhibit high selectivity for the reduction of CO_2 to CO. A new study shows that alloying Pd with Cu can suppress hydrocarbon production as well as efficiently enhance CO production to over 85% faradaic efficiency.[90] Compared with bulk Cu catalysts, the DFT calculations show that the PdCu alloy can increase the energy barriers to the CO* protonation step, and thus suppress the conversion of CO_2 to hydrocarbons. In another report, the highly selective CO production over PdCu alloy catalysts is attributed to an optimum ratio of Cu atoms and low-coordination sites of Pd atoms. Similarly, the ordered PdCu catalyst is shown to exhibit higher CO selectivity than the phase-segregated or disordered PdCu catalysts.[91]

Mechanistic understanding of the alloy effect on catalytic activity and selectivity is also achieved by a combination of experimental and theoretical studies of PdCu bimetallic alloy catalysts for CO_2 hydrogenation to methanol. The formation of the Cu alloy in catalysts is also another efficient strategy for improving the catalytic performance for methanol synthesis from CO_2 hydrogenation. For example, Jiang *et al.* reported that there were high methanol formation rates over silica-supported PdCu catalysts, which was ascribed to a strong synergistic alloy effect between Pd and Cu.[92] Nie *et al.* performed DFT calculations to investigate the mechanism of the alloy effect of PdCu catalysts for CO_2 hydrogenation to methanol (Fig. 11a and b).[93] The results suggested that the PdCu alloy showed promising capability for the adsorption and activation of CO_2 and H_2 during CO_2 hydrogenation to methanol. And the conversion of CO_2 to methanol over the PdCu alloy preferred the formate pathway ($CO_2^* \rightarrow HCOO^* \rightarrow HCOOH^* \rightarrow {}^*H_2COOH \rightarrow {}^*CH_2O \rightarrow {}^*CH_3O \rightarrow {}^*CH_3OH$), whereas the RWGS (reverse water-gas shift reaction) + CO-hydro pathway (${}^*CO_2 + {}^*H_2 \rightarrow {}^*CO + H_2O \rightarrow CHO \rightarrow {}^*CH_2O \rightarrow {}^*CH_3O \rightarrow {}^*CH_3OH$) more easily stayed at the formation of CO (Fig. 11c).

Similar approaches have also been used to study the active sites on CuSn alloy catalysts for selective electroreduction of CO_2 in aqueous solutions. CuSn alloy catalysts have been investigated to achieve the efficient and selective reduction of CO_2 to CO.[94,95] For example, Takanabe *et al.* electrodeposited Sn species on the surface of oxide-derived copper to obtain a CuSn bimetallic alloy catalyst, which showed >90% faradaic efficiency for CO over a wide potential range (−0.4 to −0.8 V *vs.* RHE) for a long time (>14 h).[41] The formation of CuSn bimetallic alloy phases is confirmed by XRD characterization. DFT calculations show no dramatic shifts in the bulk electronic structure after a Sn atom replaces a Cu atom. The introduction of Sn on reduced oxide-derived Cu is not conducive to hydrogenation because the active sites on the CuSn alloy catalysts inhibit adsorbed H*, further improving the CO faradaic efficiency. The theoretical thermodynamic studies from DFT calculations reveal the active species, synergistic interaction and reaction mechanism of copper-alloy catalysts. Combining Sn with Cu to form CuSn catalysts is another powerful way to enhance the selectivity and activity for CO_2 reduction to formate by bringing an extra synergistic effect or stabilizing the reaction intermediates.[96] Recently, relevant work involving CuSn heterostructure, CuSn core–shell structure, CuSn alloy catalysts, *etc.* has been widely reported, showing improved performance for CO_2 reduction to formate.[96]

The CuCo alloy is an intriguing catalyst for syngas (CO + H2) conversion towards higher alcohols, which is demonstrated in a recent DFT and microkinetic modeling study of the formation of methane, methanol, and ethanol from syngas on a close-packed CuCo(111) and a stepped CuCo(211) surface.[97] A structure sensitive selectivity is revealed. The CuCo(211) surface is selective toward ethanol, whereas the CuCo(111) surface is selective toward methanol. The origin of the high selectivity toward ethanol on the (211) surface is attributed to the combination of the much lower C–O dissociation barrier and the higher rate of the CH_x–CO coupling reaction.

Insights into the mechanism for reduction of CO_2 to methanol have been greatly advanced with a deeper understanding of the active species as well as the formation of intermediates from experiments and DFT calculations. More recently, the electrochemical reduction of CO_2 to methanol in aqueous solutions has also attracted a great deal of interest.[98–100] One example involves $Cu_{2-x}Se$ (x = 0.3–0.4) nanocatalysts for electrochemical reduction of CO_2 to methanol with a selectivity of 77.6%,[101] and PdCu alloy aerogel for electrochemical reduction of CO_2 to methanol.[102] In addition, first-principles calculations predict that the CuCo single-atom alloy could be a promising catalyst for electrochemical reduction of CO_2 to methanol through lowering the reaction barrier by tuning the d-band of Co and Cu atoms.[103]

These studies on computationally-screened copper-alloy catalysts for enhanced catalytic activities have focused on discovering superior catalysts in heterogeneous catalysis. The reaction free energy for the elementary steps, activation energy barriers and reaction kinetics which are related to the production of intermediates can be acquired by first-principles calculations. Combined with experimental effort, the discovery of the reaction pathway and mechanistic understanding have taken a big step forward with the assistance of the above information from DFT calculations.

3. *In situ/operando* characterization

One of the longstanding problems in catalysis is the understanding of the impact of the dynamic evolution and change of atomic arrangements on the surface of a catalyst on the catalytic reaction. For copper-alloyed catalysts, the microscopic visualization and differentiation of surface atoms on single-crystal facets or thin film substrates have endowed researchers with the ability to address this problem by monitoring the surface sites in correlation with the catalytic mechanism. In some of the recent studies, the atomic-scale details of chemical structures and active surface sites involved in the reactions have been uncovered using high-resolution AP-STM (ambient pressure STM) and HP-STM (high-pressure STM) imaging tools for the characterization. The characterization allowed researchers to investigate the chemical nature of adsorption sites, molecular-scale interaction, and reaction intermediates in relation to the catalyst composition and structure. The results have shed light on the nanoscale alloying mechanism, catalytic synergy, and catalytic mechanism of copper-alloy catalysts, which are significantly different from those of the monomeric copper or copper oxide counterparts as discussed in the earlier section.

3.1. Atomic-scale morphological changes in catalytic processes

Using the STM technique, the nature of the H and CO adsorption sites has been examined for probing the synergistic interaction of H and CO on the active sites of single-atom Pt/Cu alloy catalysts.[104] For example, as shown in Fig. 12a, clusters of mobile depressions are observed on the Cu surface. H adatoms are detected on the terraces. The adsorbed H on the surface is removed upon increasing the bias to 200 Mv (Fig. 12b). The adsorbed CO is also removed after applying 5 V pulses. Individual Pt atoms were revealed underneath each removed CO molecule, suggesting that CO is selectively adsorbed on the Pt sites. The strategy of preparing the single-atom Pt alloy reduces the binding

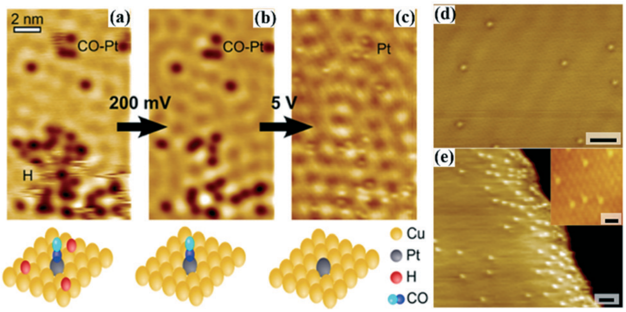

Fig. 12 STM images of (a) H and CO adsorbed on the Pt–Cu(111) SAA surface, (b) remove adsorbed H on the surface and (c) remove adsorbed CO, individual Pt atoms are present underneath each removed CO molecule. Reprinted with permission from ref. 104. Copyright 2016 American Chemical Society. (d) STM image of the Pt/Cu(111) single-atom alloy surface. Scale bar: 1.5 nm. (e) Wide-scale image of the Pt/Cu(111) single-atom alloy surface. Scale bar: 1 nm. Insert: Atomic-resolution image of the alloy surface. Scale bar, 0.5 nm. Reprinted with permission from ref. 105. Copyright 2018 Springer Nature.

strength of CO on the surface of the catalyst and enhances the ability of CO tolerance in the reaction of selective hydrogenation from acetylene to ethene. In Sykes's group, STM is also applied to investigate the alloying mechanism and coke-resistant property of Cu-based catalysts.[105] The Pt/Cu single-atom alloys function as coke-resistant catalysts under realistic operating conditions for C–H activation. It can be observed from Fig. 12d that Pt atoms in the alloys are monodispersed on the Pt/Cu(111) surface. In the wide-scale image (Fig. 12e), Pt atoms are distributed on both the terraces and the regions near the step edges. The Pt/Cu single-atom alloy is found to be more efficient than Cu for C–H activation and for coke resistance.

The STM identification of the single-atom alloy sites reveals spillover of hydrogen atoms from the Pt site to Cu sites for selective hydrogenation and CO adsorption on alloy sites. The atomic-scale visualization of the catalytic activities on the surface derived using copper as host atoms for Pt atoms,[39,104,105] as pioneered by Sykes' group, has paved the way to single-atom alloy catalysis in a significant way. Dispersing catalytically active metal atoms in a host of metal atoms at the single-atom level allows the dissociation and reaction sites to be decoupled which facilitates facile dissociation of reactants to achieve efficient and selective activity.

In situ AP-STM has been used to acquire detailed information of atomic-scale active surface sites which provides an insight into the catalytic mechanisms during the reaction. For instance, Fig. 13a and b display the STM image of the CuCo surface at atom resolution under 3 Torr CO.[106] It can be observed that the clusters are present as dimer rows, which appear as pairs of bright spots along the [110] direction. The 3.5 Å distance is larger than the atomic lattice spacing of 2.55 Å of cobalt. However, the periodicity of 3 Å in the [001] direction is less than the atomic periodicity of 3.61 Å of copper. As shown in the model of Fig. 13c, 1.75 CO molecules per Co site and 0.19 CO per Cu site are estimated.[106] It is proposed that multiple CO adsorptions on a single Co site can reduce the probability of C–O bond cleavage by weakening the M–CO bond, which can explain why the CuCo alloy has higher selectivity toward oxygenated products in the Fischer–Tropsch synthesis.

The origin of the thickness-dependent oxidation of ultrathin Cu films was investigated on Cu–Au alloy catalysts, aiming to reveal the active sites and structure–function correlation in heterogeneous catalysis. The oxidation resistance of ultrathin Cu films has been an interesting research hotspot. Herein, microscopic and visual understanding *via* the STM technique is demonstrated at an atomic scale from ultrahigh vacuum to near ambient conditions.[107] As shown in Fig. 14, monolayer (ML) and multilayer Cu/Au(111) model catalysts were used. The strong interfacial interaction between Cu and Au enhances the stability of ultrathin Cu films on the surface of alloy catalysts, displaying a thickness-dependent surface structure. The sequence of oxidation resistance is Cu(111) $<$ 2.4 ML Cu $<$ 0.4 ML Cu $<$ 0.4 ML Cu (annealed at 600 K). At O_2 pressure below 10^{-4} mbar, the formation of copper oxides is prevented *via* subsurface diffusion of Cu and the formation of a Au-rich surface alloy. However, CuO appears under near ambient conditions for 0.4 ML Cu. Furthermore, increasing the annealing temperature to 600 K inhibits the formation of copper oxides due to Cu diffusion to the bulk substrate. The findings provide insight into the evolution of copper-alloy catalysts from ultrahigh vacuum to near ambient conditions.

Likewise, the growth of copper oxide thin films as reactive sites was probed on the surface of Cu–Pt alloy catalysts, using STM, XPS and electron diffraction. In the case of Cu–Au alloy catalysts, Cu which is capable of gradually diffusing to the bulk Au substrate with increasing annealing temperature to 600 K. Pt (111), with a similar lattice parameter to Au, was

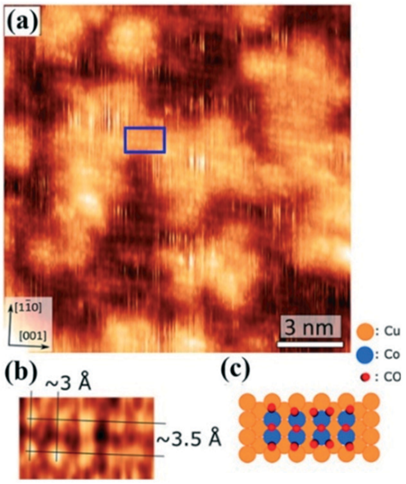

Fig. 13 (a) STM image of the CuCo surface in the presence of 3 Torr CO. (b) The expanded area of (a). (c) The surface structure of a proposed model. Reprinted with permission from ref. 106. Copyright 2018 American Chemical Society.

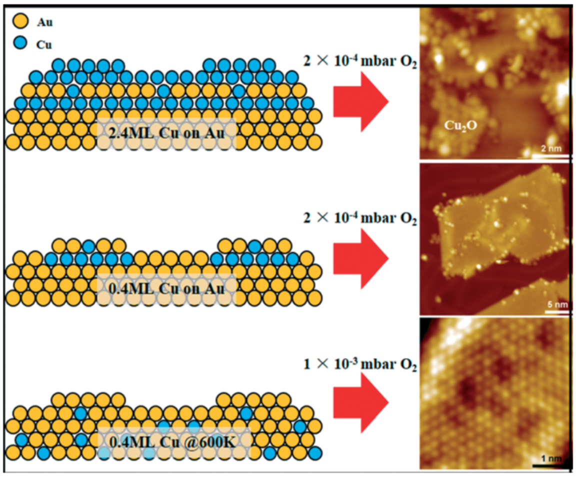

Fig. 14 Schematic diagram of the thickness-dependent oxidation kinetics of Cu layers on Au(111). Reprinted with permission from ref. 107. Copyright 2018 American Chemical Society.

used to replace Au (111) as a substrate to study the morphology, growth and electronic structure of copper oxide thin films on the surface of alloy catalysts.[108] The Cu–O films are grown on a slab of Cu (111) at the Pt interface at low temperature. The microscopic structures are like the "29" and "44" configurations from Cu (111) oxidation, judging from the size of their unit cells. With increasing preparation temperature, the surface oxide goes through an order–disorder phase transition, and a well-ordered Cu_3Pt alloy appears on the surface. At high temperature, Cu_3O shamrock units assemble into a well-ordered $2\sqrt{3}$ phase on the surface, which is a unique network on the Pt(111) support.

The reactivity and mechanism for the conversion of methanol and methanol–water mixtures to formaldehyde are studied over catalysts with oxygen-free Cu (111) and Pd/Cu (111) alloy surfaces.[109] Methoxy is grown on the flat Cu (111) surface, and water inside hydrogen-bonded networks binds a proton to drive OH bond scission. The introduction of isolated Pd atoms near the Cu step edges improves the stability of methanol on the Pd-rich areas at step edges, inducing more OH bond activation on the Cu (111) surface. Six or more water molecules collectively work to deprotonate methanol to methoxy, which is stabilized at Cu step edges and/or Pd atoms to selectively form formaldehyde at higher temperatures. The results show that over a Pd/Cu alloyed surface, water is capable of deprotonating methanol into methoxy at low temperature, and then methoxy further dehydrogenates to form formaldehyde on the surface of catalysts.

Due to limitations in terms of relatively low pressure and low temperature for AP-STM to operate, it is challenging to obtain information for assessing the temperature/pressure dependence of the atomic-scale surface structures and active sites of the catalysts. Nevertheless, the advances in AP-STM or HP-STM have made it possible to visualize the atomic-scale details of the surface and interface structures and the reaction intermediates at certain reaction pressures and temperatures. Moreover, the presence of gas reactants not only alters the morphology and chemistry on the catalyst surface, but also changes the oxidation states of surface species as a result of adsorbate–catalyst interaction, which are subjects of further AP-STM or HP-STM investigations.

The observation of the atomic-scale morphological changes of copper-alloyed catalysts in real-time aids the understanding of how the alloyed-copper surface undergoes dynamic changes under the reaction gas atmosphere. Recently, environmental transmission electron microscopy (ETEM) was used to visualize the dynamic evolution of the atomic adlayer over CeO_2-supported AuCu catalysts under CO oxidation conditions operated at 0.01 mbar pressure.[110] The *in situ* experiment involved the use of the (010) surface of a $AuCu/CeO_2$ catalyst and HRTEM with fast Fourier transformation (FFT) analysis capability. Luo *et al.* found that the AuCu alloy features an FCC alloying characteristic and is terminated by {111} and {010} surfaces.[110] Compared to intact {111} surfaces, an atomic "adlayer" was formed over {010} surfaces under a CO + O_2 atmosphere, reflecting a strong interaction with gas molecules through Au–CO bonding at low-coordinated surface metal atoms and a dynamic evolving structure with no fixed distance between atoms. DFT calculation was also used to understand whether Au or Cu tends to segregate to the subsurface during the oxidation reaction. The results show that the adsorption energy of CO on both flat and stepped AuCu1-sub (100) is stronger than that on AuCu1-sur (100), indicating that Cu tends to remain at the subsurface sites upon CO adsorption. This finding provides an important insight into the atomic mobilities on the surface and subsurface of AuCu alloy nanoparticle surfaces.

3.2. Structural evolution and dynamic reconstruction

The surface atoms or structures of a catalyst are highly dynamic under catalytic reaction conditions. However, fundamental understanding of how the atoms on the copper alloy surface operate synergistically with noble transition metals in the highly-dynamic process of phase structure, chemical ordering/disordering, lattice straining during catalytic reactions has been very challenging. Recent studies have provided some insights into this understanding for copper nanoalloy catalysts, which have relied largely on *in situ*/*operando* studies of the nanoscale composition, nanocrystal structure and phase structure transformations of catalysts in heterogeneous catalysis.[111–114] Among the different studies, *in situ*/*operando* HE-XRD is a powerful tool for unraveling crystalline structure and phase properties in correlation with the catalytic activity of the catalysts during the reaction. The coupling of HE-XRD to PDF analysis provides the ability to reveal the phase structural evolution of catalysts with atomic level details under the reaction atmospheres.[28,115–118] The *in situ*/*operando* XRD/PDF technique has also been used in combination with other characterization techniques (*e.g.*, DRFITs, EDS mapping, *etc.*) for providing an in-depth understanding of structure–reactivity correlations under reaction conditions.

The evolution of the phase state of PdCu alloy NPs thermally sintered from mixed Pd and Cu NPs is monitored in real-time using *in situ* synchrotron XRD. The conditions involve isothermal heating under a He atmosphere at 300 °C (a) and then heating under a H_2 atmosphere (b) to 700 °C (Fig. 15).[65] A chemically ordered bcc (B2-type) alloy phase is formed from Pd and Cu NPs at 300 °C, He (Fig. 15a). At 450 °C, H_2, a chemically dis-ordered (fcc-type) alloy phase is formed. Both chemically disordered and ordered PdCu nanoalloy phases coexist up to 700 °C, H_2 (Fig. 15b). Mukundan *et al.*[116,117] further showed that the combination of metal–support interaction and reactive/non-reactive environment influences the thermal structural evolution and ultimate structure of the nanoalloys formed from the Pd and Cu nanoparticles. This finding demonstrates not only the propensity of Pd–Cu nanoalloy formation from heating a mixture of Pd and Cu nanoparticles but also the dynamic nature of the phase structure under heating conditions.

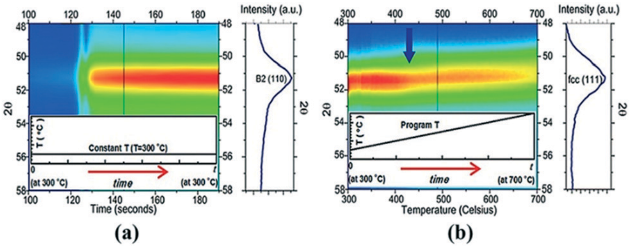

Fig. 15 Evolution of the intensity of peaks in the XRD patterns over the PdCu catalyst. (a) Formation of the chemically ordered B2-type phase under a He gas atmosphere. (b) Transformation of the B2/bcc alloy phase into a chemically disordered fcc-type alloy phase under a H_2 atmosphere. Reprinted with permission from ref. 65. Copyright 2015 The Royal Society of Chemistry.

The detailed structural evolution of the alloy catalyst during thermochemical treatments was further monitored by *in situ*/*operando* synchrotron HE-XRD/PDF measurements (Fig. 16A).[65] Starting with a fresh PdCu nanoalloy catalyst characteristic of a single-phase alloy, the heating treatment under O_2 is shown to induce phase segregation at 400 °C, which is enhanced upon cooling back to room temperature (Fig. 16B-a). As shown in experimental atomic PDFs (Fig. 16B-b), the first peak for the fresh $Pd_{21}Cu_{79}/C$ catalyst is symmetric and positioned at about 2.58 Å that is very close to the first neighbor Cu–Cu distance in bulk Cu (2.56 Å). At 400 °C, the first PDF peak splits into two components positioned at 2.78 Å and 3.25 Å, respectively, indicating nanophase segregation. The phase state depends on the bimetallic composition, as evidenced by the observation of phase segregation at a Pd : Cu ratio of ∼50 : 50 whereas a single phase is observed with lower or higher Pd : Cu ratios. This finding demonstrates that the phase state and the atomic-scale structure can be changed by either changing the bimetallic composition and/or by thermochemical treatment, which constitutes important pathways for fine-tuning the catalytic properties of nanoalloys.

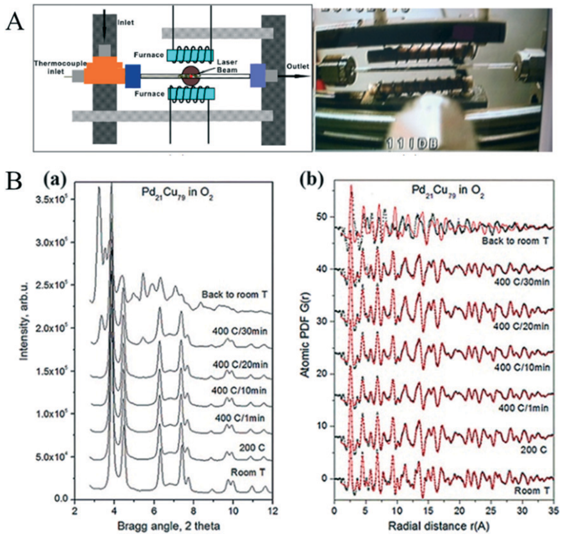

Fig. 16 (A) The experimental setup for a gas flow/furnace/sample cell used in the *in situ* HE-XRD experiment. (B) *In situ* HE-XRD/PDF data: (a) HE-XRD patterns obtained upon heating $Pd_{21}Cu_{79}/C$ under O_2 to 400 °C; (b) the respective experimental PDFs (symbols) with the corresponding fitting curves (red lines). Reprinted with permission from ref. 65. Copyright 2015 The Royal Society of Chemistry.

Another example of *in situ* HE-XRD/PDF characterization involves the study of copper-alloy catalysts under a O_2 or H_2 atmosphere at different temperatures, revealing nanostructural alloying and evolution. In a recent study, the phase structures of AuCu alloys thermochemically treated under an oxidative or reductive atmosphere are examined.[109] The nanoalloy features high crystallinity and multiple facets, and the detected Cu and Au concentrations in the nanoparticles show a good degree of alloying across the entire nanoparticle. As shown in Fig. 17A, a lattice "expanding–shrinking" phenomenon is revealed by the PDF data for the AuCu alloy catalyst upon the oxidative and reductive thermochemical treatments. The degree of the lattice expansion and shrinking depends on the composition of the alloy catalyst. The catalyst after reductive treatment displays a better catalytic performance for CO oxidation than the catalyst after oxidative treatment. A partial melting and re-solidification mechanism are proposed to realize nanoscale alloying and structural evolution toward an fcc-type nanoalloy. The presence of bifunctional sites on the nanoalloy surface is believed to enhance the catalytic activity for CO oxidation.

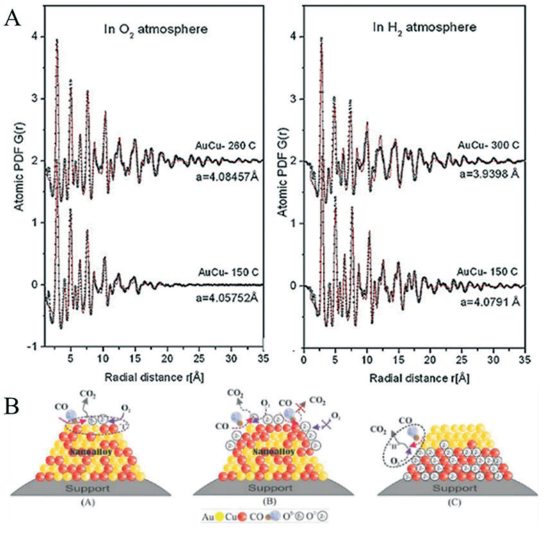

Fig. 17 (A) Atomic PDFs for the $Au_{51}Cu_{49}/C$ catalyst under oxidative (O_2) and reductive (H_2) atmosphere. The symbols represent the experimental data; the red lines represent the computed data based on an fcc-type structure. (B) Illustration of surface sites for oxygen activation on a supported AuCu catalyst in either reduced (A) or oxidized nanoalloy (B) states, where Cu provides sites for surface oxygenation involving O^{2-} and $O^{\delta-}$ species and phase-segregated state (*i.e.*, Au NPs supported on CuO_x) (C) ("I" site for O_2 activation exists largely on the reduced nanoalloy surface (case a), not on the oxidized one where the surface is completely blocked by the oxide species (O^{2-}, case b). "II" sites for O_2 activation exist for case C). Reprinted with permission from ref. 52. Copyright 2012 American Chemical Society.

The finding from the *in situ* HE-XRD/PDF characterization provided some clues for understanding the catalytic synergies of the AuCu catalysts for CO oxidation (Fig. 17B). The bifunctional active sites mentioned above are strongly dependent on the thermochemical treatments. The CO oxidation over AuCu nanoalloy catalysts is shown to depend on the degree of surface oxygenation.[52] While the activity of the catalyst treated in O_2 (deep surface oxygenation) was low, the activity is significantly increased upon a reduction treatment of the catalyst in H_2 (light surface oxygenation). This finding indicates that light surface oxygenation (under CO + O_2 reaction conditions) of the nanoalloy increases the activity, reflecting the role of surface oxygenated species on the Cu species in the reaction, as supported by the *in situ* HE-XRD/PDF analysis.[118] It provides oxygen storage and release capacity, creating bifunctional surface sites where the Au-site activates CO, whereas the oxygenated base metal activates oxygen. The copper species in the AuCu nanoalloys provide activated $O^{\delta-}$ species in the oxidation reaction of CO under the conditions of <90% Cu in the AuCu alloy. This type of O_2 activation site exists largely on a reduced nanoalloy surface (Fig. 17A, left). Upon oxidation, the surface is completely blocked by oxide species (Fig. 17A, right). When Cu is >90%, the alloy either does not exist on the oxidized nanoparticle surface, or the oxygenated copper species undergo phase segregation to produce CuO_x supported Au nanoparticles where certain Au sites on the surface are fully surrounded by CuO. This result demonstrates that the degree of surface oxygenation of AuCu nanoalloys plays an important role in the activation of oxygen species for the CO oxidation reaction.

The *in situ* HE-XRD/PDF technique has also been utilized to study the crystalline structural evolution of the nanoalloy catalysts inside a fuel cell under the operating conditions (Fig. 18A). One example involves the study of fresh and potential-cycled $Pt_{37}Ni_{29}Cu_{34}$ alloy catalysts in a fuel cell, in which the PDF data reveal a change of the catalyst from fcc to a mixture of tetragonal and fcc phase structures (Fig. 18B-a). Fig. 18B-b shows nanophase analysis, color maps of the phase content and corresponding reactivity of the $Pt_{37}Ni_{29}$-Cu_{34} alloy nanocatalyst *vs.* time of electrochemical cycling.[26] $Pt_{37}Ni_{29}Cu_{34}$ experiences weight loss of Cu and Ni species and segregates into a mixture phase of tetragonal (44 vol%) and cubic-type (56 vol%) in about 1 h, and tetragonal (41 vol%) and cubic-type (59 vol%) in about 6 h. Both the structure type of the fresh Pt–Ni–Cu alloy and the trajectory of structural phase transformation under operation conditions reflect the phase diagram of the bulk alloys. The *in situ*/*operando* evidence of the structural evolution provides an insight into the nanophase structures in correlation with the activity and stability of the alloy catalysts.

Analyses of the *operando* PDFs also provide insights into the correlation between the nanostructure and the electrocatalytic performance of the catalyst in a fuel cell. For example, the Pd–Cu nanoalloy with a chemical composition close to Pd_1Cu_1 is shown to exhibit higher catalytic activity than Pd_1Cu_2 and Pd_3Cu_1 for the oxygen reduction reaction (ORR). PDF analysis of the *in situ*/*operando* HE-XRD data indicates that the structural changes of Pd–Cu nanoalloys during the reaction result in the decay of the catalytic activity.[119] There is a link between the ever-adapting structural state of the Pd–Cu catalyst and the catalytic performance.[120] The $Pd_{50}Cu_{50}$ nanoalloy with a mixed phase of bcc and fcc shows the optimal catalytic activity among Pd_n-Cu_{100-n} nanoalloys with different compositions, which gradually changes to a single-phase upon potential cycling under ORR conditions.[120] The degree of Cu dissolution in the nanoalloys depends on the composition, phase state and surface properties of the PdCu catalysts.

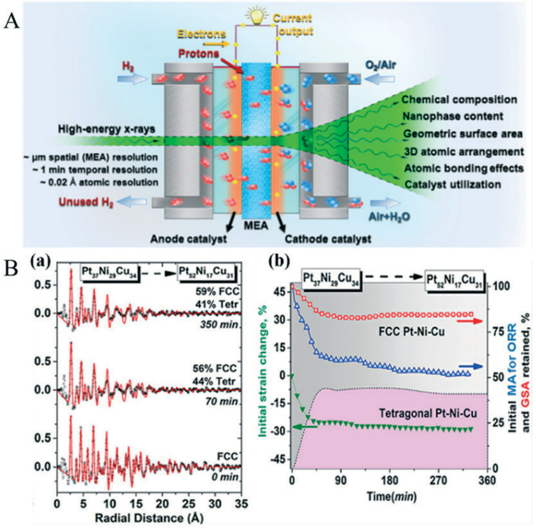

Fig. 18 (A) Illustration of the setup for the *in situ*/*operando* HE-XRD measurement of the catalyst in a PEM fuel cell. (B) (a) *Operando* HE-XRD/PDF data for fresh and potential-cycled $Pt_{37}Ni_{29}Cu_{34}$ alloy catalysts in a fuel cell. Experimental PDFs (black line) are matched with computed PDFs (red line) derived from models. (b) Plots of lattice strains and color maps for the phase content of the alloy catalyst *vs.* time of potential cycling. The retention of the initial GSA (geometric surface area, red) and effective MA (mass activity, blue) of the catalyst for the ORR (oxygen reduction reaction) are included in the plots. The composition change by potential cycling is indicated in the upper part of the plots. Reprinted with permission from ref. 26. Copyright 2018 Elsevier.

In situ/*operando* HE-XRD coupled to atomic PDF_S analysis reveals the detailed phase-type and atomic arrangement of copper-alloy catalysts. The information obtained from the use of this technique would also be useful for understanding the results from *ex situ* studies involving alloys of lighter group 11 elements Cu and Ag that are not only more prone to size change but also more structurally disordered at the nanoscale than heavier group 11 elements such as Au,[121] and the molecule-solid duality concept for nanoscale control of size, shape and alloying is revealed for binary copper gold nanoclusters or nanoparticles towards alloy nanocubes.[122] The B2 phase in PdCu 3:1 mixtures dominates after isothermal annealing at 450 °C, but a significant disordered alloy fcc phase is also formed. The B2 phase transforms into

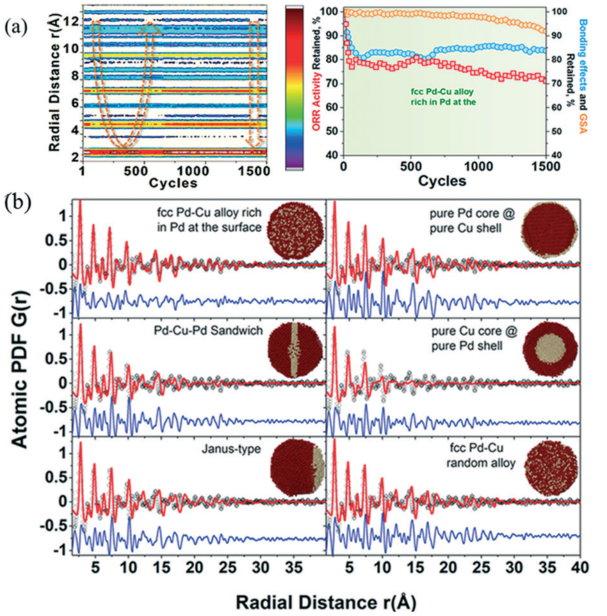

Fig. 19 (a) (left) Color map of the low-*r* part of the *in operando* atomic PDFs for $Pd_{75}Cu_{25}$ alloy NPs. The U-shaped arrow highlights the sequence of abrupt dips and rises in the intensity of several PDF features occurring within the initial 700 PEMFC cycles. The vertical arrow highlights another abrupt drop and rise in the intensity of the same features this time occurring after 1200 PEMFC cycles. The highlighted PDF changes can be related to distinct stages in the evolution of the ORR (MA) activity of $Pd_{75}Cu_{25}$ NPs during the PEMFC operation, as discussed in the text. (right) Change in the ORR (MA) activity (red squares) and GSA (orange rhombs) of $Pd_{75}Cu_{25}$ NPs during 1450 PEMFC cycles. The NPs remain single fcc Pd–Cu nanophase rich in Pd at the surface throughout the PEMFC cycling. (b) Exemplary experimental and simulated nanophase analysis for $Pd_{75}Cu_{25}$ NPs that underwent 1450 PEMFC cycles (insert: snap-shots of the respective nanophases). Reprinted with permission from ref. 119. Copyright 2018 Royal Chemical Society.

a disordered fcc alloy at higher temperatures (>450 °C). During annealing at 750 °C, the disordered fcc phase grows at the expense of the B2 phase.[116] Pd and Cu atoms in the PdCu nanoalloy display crystal structures in ordered bcc and disordered fcc.[123] These findings are valuable for exploiting the unique catalytic properties of copper-alloy catalysts, finding opportunities for fine-tuning the structure, and inspiring future effort toward the search for superior alloy catalysts.

Recently, the change of nanoscale phase structure of $Pt_{75}Cu_{25}$ alloys during PEMFC operation was explored by a "search and match" procedure using *in situ* PDFs (Fig. 19a).[119] Through "matching" atomic PDFs computed from the model nanophases of Pd_3Cu_1 and the experimental PDF for $Pd_{75}Cu_{25}$ alloys that underwent 1450 potential cycles under PEMFC operation, it reveals that the NPs feature an fcc Pd–Cu alloy whose surface is enriched with Pd (Fig. 19b). During potential cycling, the $Pt_{75}Cu_{25}$ alloy was shown to experience significant intermittent fluctuations. However, it largely preserved the fcc alloy type structure depending on the bimetallic composition. The leaching of Cu species from the NPs was shown to induce losses in the ORR activity and atomic-scale changes of Pd–Cu alloy NPs, including changes in the relative phase composition, GSA and bonding distances. These changes were found to be highly correlated (Fig. 19a). This finding could aid the further efforts in the design of Cu based electrocatalysts for controlling the mass transport and interdiffusion of Cu atoms in the catalyst under fuel cell operation conditions.

There are many other relevant examples involving *in situ* spectroscopic techniques for the study of Cu-alloy catalysts. For example, the local coordination structure of atoms in the alloy catalyst is examined by XAFS in terms of metal–metal coordination, metal–oxygen coordination, and metal oxidation state, providing important information for assessing the interaction between copper and other metals. Recently, an extended X-ray absorption fine structure (EXASF) study, aided by DFT calculations, has revealed the correlation of the active sites and structure with the catalytic performance for CO_2 reduction over Au/Cu alloy catalysts.[84] The Au/Cu alloy structures are emerging as a promising system for the electrochemical CO_2 reduction reaction. Kauffman *et al.* reported that the thiol-ligand plays an important role in the selectivity of AuCu bimetallic catalysts toward CO_2 reduction.[84] The studies found that the presence of Cu atoms in the ligand shell sustained the CO selectivity under the conditions of reduced precious metal amount because the copper–thiol surface structure is favorable for stabilizing key *CO intermediates rather than *H binding. Removing a significant fraction of the thiol ligands by prediction, the strength of *CO binding increases, resulting in the decrease of selectivity for electrochemical CO_2 reduction.

The findings could provide some information for assessing results from other *ex situ*/*in situ* studies. One example involves the nanoporous CuAg alloys in terms of catalytic selectivity toward C_2 products.[53,124,125] Huang *et al.* discovered the indispensable role of CuAg interface in promoting electrochemical CO_2 reduction to ethylene.[126] They developed a seeded-growth colloidal synthesis to form AgCu nanodimers with tunable Cu domain size including Ag_1–$Cu_{0.4}$, Ag_1–$Cu_{1.1}$, and Ag_1–$Cu_{3.2}$, wherein the Ag_1–$Cu_{1.1}$ catalyst reached a 3.4-fold enhancement in the faradaic efficiency for ethylene compared with the pure Cu counterpart. The enhancement could be mainly attributed to tandem catalysis and charge transfer, which were both induced by the coupling of segregated Cu and Ag atoms through their interface.

For the water-gas shift (WGS) reaction, the synergistic effect of the active surface sites on bimetallic PdCu alloy catalysts is investigated *in situ* extended X-ray absorption fine structure (EXAFS).[127,128] For example, in the study of the synergistic effects of PdCu on a hydrotalcite-carbon support on the oxygenated coupling reaction by Goulas *et al.*, the Pd–Cu alloy catalyst with a 3 : 1 ratio of Pd to Cu was shown to greatly decrease the undesirable decarbonylation reaction and maintain high catalytic rates.[129] From the X-ray absorption near edge structure (XANES) spectra of the Pd edge and Cu edge of the PdCu supported on hydrotalcite-carbon (HT) catalysts, the status of Cu is Cu^{2+}, which replaces Mg^{2+} and Al^{3+} in the HT structure, resulting in a small amount of Cu available for alloying with Pd. Interestingly, Cu preferentially alloys with Pd on carbon-supported catalysts. This finding is explained by the prevention of decarbonylation pathways from Pd sites due to the formation of the alloy and the enhancement of reactivity *via* the production of Cu sites, demonstrating the important role of the copper component in the catalytic synergy of the bimetallic catalyst in the reaction. This understanding is also useful for assessing results from other *ex situ* studies such as the rate-determining step and reaction mechanism for efficient NO reduction on Cu–Pd alloy nanoparticles,[130] where a single-atom alloy structure (*i.e.*, Pd atoms well isolated by Cu atoms) was identified upon 5 : 1 alloying which displayed excellent catalytic activity, selectivity, and stability for NO reduction by CO.

In situ EXAFS, HAADF-STEM, temperature-programmed desorption/reaction (TPD/R), and STM measurements in ultra-high vacuum (UHV) gas chambers have been used to probe the active sites on single atom alloys, *e.g.*, PtCu, for selective dehydrogenation of methanol to formaldehyde and hydrogen.[131] The first commercial production of formaldehyde began in 1890 *via* methanol dehydrogenation by using a copper catalyst. For methanol dehydrogenation to formaldehyde, iron and molybdenum-based catalysts are widely used.[109,132–135] However, the current commercial catalysts need oxygen to facilitate methanol dehydrogenation. Formaldehyde is required to separate from water for application as an intermediate, and it is an energy-consuming process.

The Cu-based catalyst has also shown promise to play a role in methanol dehydrogenation to formaldehyde in the absence of oxygen.[64,136–138] In this work, small amounts of highly-dispersed isolated Pt atoms form PtCu single atom alloys on the Cu surface, which are the active sites for dehydrogenation of methanol to formaldehyde and hydrogen in the absence of oxygen adatoms. The studies found that the highly-dispersed isolated Pt atoms have a significant promotional effect on the catalytic performance under realistic reaction conditions, which is attributed to the stabilization of H atoms by water, resulting in methanol dehydrogenation to methoxy, and then further to formaldehyde. The discovery has practical value for exploring the active sites and reaction mechanism under realistic reaction conditions.

The ability to detect atomic-scale phase separation and clustering of solute atoms in AuCu alloys was recently demonstrated by Zhou's research group. Their measurements involved *in situ* dynamic, atomic-scale electron microscopy observations and theoretical modeling.[139] The disparity in the adatom–substrate exchange barriers is shown to separate Cu adatoms from a Cu–Au mixture, forming a fluid phase enriched with Au adatoms towards clusters. The atomic-scale mechanism is associated with the nucleation, rotation and amorphization–crystallization oscillations of the Au clusters. As shown by the *in situ* HRTEM images of the nucleation of crystalline Au clusters on the edge along the (110) facet of the substrate in Fig. 20, the aggregation of Au adatoms results in a small cluster that remains noncrystalline (Fig. 20a and b). Upon growing the cluster larger than 2 nm, it transforms into a crystalline state (Fig. 20c and d). The as-crystalized clusters are randomly oriented, and undergo gradual rotation to align with the substrate (Fig. 20c–e), *i.e.*, (111)Au//(220)Cu(Au). The cluster size is shown to play a significant role in controlling the amorphous-to-crystalline phase transition and the cluster rotation kinetics.

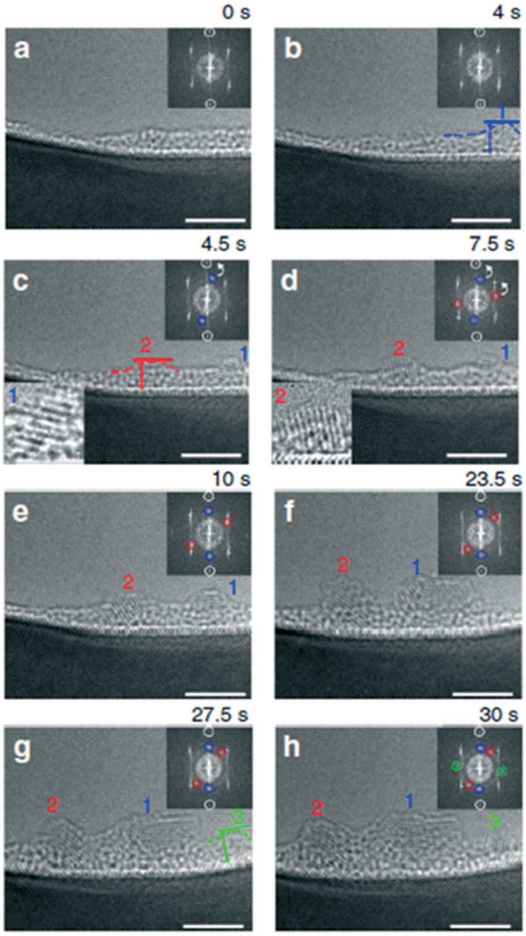

Fig. 20 *In situ* HRTEM images of the AuCu alloy substrate at 600 °C and 1×10^{-3} Torr of H_2 gas flow, showing amorphous-to-crystalline transition and grain rotation of Au clusters. a–d) The aggregation of Au atoms results in the formation of clusters 1 and 2 that subsequently transform into a crystalline state with the appearance of Au(111) lattice planes and cluster rotation. e and f) Growth of crystalized clusters, where cluster 1 stays relatively stationary, while cluster 2 undergoes slow rotation. The insets in c and d are the zoom-in view showing the presence of crystalline lattice in clusters 1 and 2. g and h) Nucleation and growth of cluster 3 followed by subsequent amorphous-to-crystalline transition and grain rotation. Scale bar, 4 nm (a–h). Reprinted with permission from ref. 139. Copyright 2020 Springer Nature.

In the latest DFT and *in situ* HRTEM study,[110] CO adsorption is shown to induce Au segregation on the AuCu

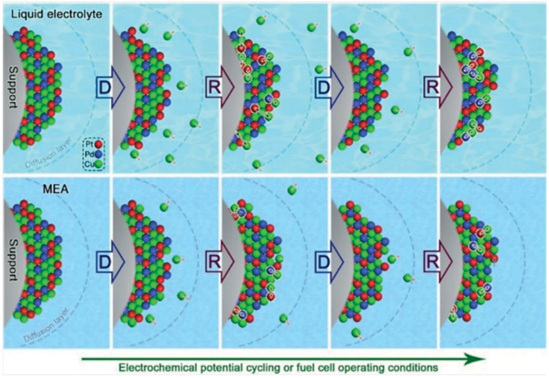

Fig. 21 A schematic illustration of the realloying process in the PtPdCu nanoalloy as a result of dealloying in the liquid cell (top panel) and the membrane electrode assembly (bottom panel). Reprinted with permission from ref. 141. Copyright 2021 Springer Nature.

nanoparticle surface. The O_2 dissociative adsorption leads to oxidation of Cu and segregation of subsurface Cu to the surface sites, which provides extra active sites (Au-rich).[140] This finding provides strong evidence for the highly-dynamic nature of the AuCu nanoparticle catalysts.

The structure durability of copper-containing nanoalloy catalysts has also been probed by *in situ*/*operando* HE-XRD/PDF. One recent example involves the study of the $Pt_{20}Pd_{20}Cu_{60}$/C catalyst in terms of compressive strain and high durability,[141] revealing the operation of dynamic realloying in the catalyst under fuel cell operating conditions (Fig. 21). The partial dissolution of Cu into the electrolyte during the initial potential cycles is followed by a realloying process, leading to a highly effective self-healing process that realloys the remaining metals in the partially dealloyed NPs toward a thermodynamically-stable alloy. Understanding the universal nature of the dynamic self-healing process has implications for advancing nano-engineered alloy catalysts and achieving low-cost, active and stable alloy electrocatalysts for fuel cells. As demonstrated by the DFT calculations, the participation of Cu in the catalyst greatly reduces the activation barriers for some key elementary steps during the ORR, boosting the reaction energetics.

The exploration of the realloying synergy depends heavily on the understanding of the dynamic atomic-scale structural change of metals in the nanoalloys under reaction conditions,[142,143] including reaction temperature, surface adsorbate, chemical environment, applied electrochemical potentials, *etc.* The dynamic evolution of the core–shell/alloy structures under the reaction conditions plays a crucial role in the catalytic performance of the nanocatalysts. In this regard, the employment of advanced techniques, especially *in situ*/*operando* synchrotron high-energy X-ray diffraction and pair distribution functional analyses, provides significant insights into the highly dynamic processes.

AP-XPS is a powerful technique for gaining an insight into the surface species on the catalyst. For example, AP-XPS was applied to study the adsorbates and chemical states of elements on the surface of copper zinc alloy catalysts under the reaction conditions. For example, CO_2 activation and reaction over Zn-deposited copper catalysts, *e.g.*, Zn(0.31 ML)/Cu(111), were systematically studied by AP-XPS[144] in the temperature range of 299 to 473 K (0.8 mbar CO_2 + 0.4 mbar H_2 + 0.05 mbar D_2O) (Fig. 22).

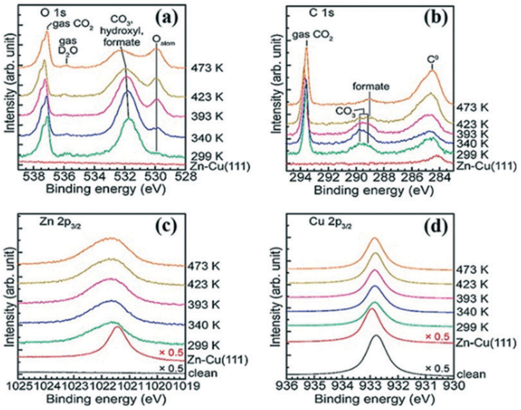

Fig. 22 AP-XPS spectra of the Zn(0.31 ML)/Cu(111) surface under 0.8 mbar CO_2, 0.4 mbar H_2, and 0.05 mbar D_2O: (a) O 1s, (b) C 1s, (c) Zn $2p_{3/2}$, and (d) Cu $2p_{3/2}$. Reprinted with permission from ref. 144. Copyright 2019 American Chemical Society.

There are two adsorbate peaks in the O 1s spectra (Fig. 22a). The wide peaks at 532.2 eV are attributed to CO_3^{2-}, hydroxyl or formate. The peak at 529.9 eV corresponds to the O atom from the ZnO overlayer. In the C 1s region (Fig. 22b), the peak at 289.0 eV is assigned to formate (HCOO), which is an intermediate for CO_2 hydrogenation. Zn is oxidized by the adsorbates of atomic oxygen, hydroxyl, or formate (Fig. 22c), which is closely associated with the addition of water, whereas Cu maintains a metallic state (Fig. 22d). The results suggest that hydroxyl from dissociative adsorption of water is a source for CO_2 hydrogenation.

4. Summary and future perspectives

Taken together, there has been clear progress in the recent research and development of copper-alloy catalysts for a wide range of catalytic reactions. Part of the progress can be attributed to the abilities of *ex situ* and *in situ* characterizations using different advanced analytical techniques which have allowed researchers to gain insights into the detailed morphologies, structures, and surface sites of the copper-alloy catalysts. The overall progress has led to exciting opportunities of research and development in the cutting-edge areas of sustainable energy and clean environment. It also opens a new landscape for chemical feedstocks in terms of the conversion of bio-renewable fuels and the exploitation of solar energy. The exploration of these opportunities will be an important force to push the further advancement of the catalysis field to bring greater societal impact. While not exhaustive in all aspects of copper alloy catalysts in the relevant catalytic reactions, this review has tried to focus on discussing some of the representative examples involving structural characterization of the catalysts and their catalytic mechanisms by leading researchers in heterogeneous catalysis. The inclusion of the limited examples for the synthesis and application of the catalysts and the computational modeling of the catalysts mainly reflects part of the general scope of the insights from the structural characterization, rather than repeating what have been discussed in several excellent recent reviews.

The focus of structural characterization in this review is to provide a forum for researchers to discuss the fundamental issues involving the catalytic synergies and mechanisms of the copper alloy catalysts in catalytic reactions. The development and utilization of advanced analytical techniques, especially *in situ*/*operando* techniques, have played an important role in addressing the challenge, generating significant insights into the atomic/molecular level catalytic mechanisms of catalytic reactions over copper-alloy catalysts.

While significant progress has been made in the above frontiers, major challenges remain in both fundamental understanding and practical applications of copper-alloy catalysts. There are several most important issues of future studies of Cu-alloy catalysts. First, the precise identification of the active copper species and sites on the Cu-alloy catalysts remains challenging due to the propensity of the transformation of the various oxidation states such as Cu^0, Cu^{1+}, and Cu^{2+} during the heterogeneous catalytic reactions. Second, there is a clear lack of atomic-scale insights into the catalytic mechanisms for catalytic reactions over Cu-alloy catalysts, calling for further development and increased utilization of *in situ*/*operando* characterization in the investigations. Third, there is an increased need for understanding of the control over the stability of Cu-alloy catalysts synthesized by current methods, which are important for the applications of the catalysts in industrial processes. Fourth, there is a clear need to establish the correlation between the bulk structure and the surface-active sites under reaction conditions so that the desired catalysts can be prepared and controlled by design. Finally, the complexity of multiple variables that govern the dynamic surface processes, *e.g.*, dealloying, realloying and sintering, and catalytic synergies of copper-alloy catalysts, *e.g.*, bifunctional or multifunctional surface sites, is very challenging for the precise determination of the structure–composition–activity relationships.

There is a clear need of advanced characterization techniques for gaining the much needed insights. This need calls for innovative approaches to probing the complexity through effective coupling of experimental characterization and theoretical modeling towards establishing a database for the dynamic structure–activity correlation. Part of this aspect is exemplified in a latest study of the sintering process of gold–copper alloy nanoparticles on surfaces,[145] where the subtle differences in the two atoms in terms of nanoscale-enhanced atomic diffusion, surface mobility and surface interaction energies are shown, experimentally and theoretically, to contribute to the low-temperature surface-mediated sintering of the nanoparticles. Given the challenges and opportunities, further advancement of the *in situ*/*operando* characterization techniques is essential as novel and high-performance catalysts are rapidly emerging from the preparation of copper-alloy catalysts. *In situ*/*operando* characterizations will continue to play an increasingly-important role not only in the design and optimization of the catalysts for various catalytic processes in the chemical industry, but also in the emerging fronts of catalysis science for advancing the cutting-edge areas of sustainable energy and clean environment.

Conflicts of interest

There are no conflicts to declare.

Acknowledgements

CJZ acknowledges the support from the National Science Foundation (CHE 1566283, CHE 2102482, and IIP 1640669) and the Department of Energy, Basic Energy Sciences (DE-SC0006877). SHZ acknowledges the support from the National Natural Science Foundation of China (grant no. 21968020), the "Grassland Talent" Innovation Team of Inner Mongolia, and the Natural Science Foundation of Inner Mongolia (grant no. 2018MS02020 and 2018BS02008), China.

References

1 H. Ren, S. Sun, J. Cui and X. Li, *Cryst. Growth Des.*, 2018, **18**, 6326–6369.

2 M. Zabilskiy, P. Djinović, E. Tchernychova, O. P. Tkachenko, L. M. Kustov and A. Pintar, *ACS Catal.*, 2015, **5**, 5357–5365.

3 Y. Li, S. Chu, H. Shen, Q. Xia, A. W. Robertson, J. Masa, U. Siddiqui and Z. Sun, *ACS Sustainable Chem. Eng.*, 2020, **8**, 4948–4954.

4 A. F. Bais, G. Bernhard, R. L. McKenzie, P. J. Aucamp, P. J. Young, M. Ilyas, P. Jöckel and M. Deushi, *Photochem. Photobiol. Sci.*, 2019, **18**, 602–640.

5 E. E. A. P. United Nations Environment Programme, *Photochem. Photobiol. Sci.*, 2017, **16**, 107–145.

6 E. E. A. P. United Nations Environment Programme, *Photochem. Photobiol. Sci.*, 2012, **11**, 13–27.

7 J. Campos, L. S. Sharninghausen, M. G. Manas and R. H. Crabtree, *Inorg. Chem.*, 2015, **54**, 5079–5084.

8 T. R. Reina, S. Ivanova, M. A. Centeno and J. A. Odriozola, *Appl. Catal., B*, 2016, **187**, 98–107.

9 X. Wang, Y. Liu, X. Peng, B. Lin, Y. Cao and L. Jiang, *ACS Appl. Energy Mater.*, 2018, **1**, 1408–1414.

10 S. Chen, L. Li, W. Hu, X. Huang, Q. Li, Y. Xu, Y. Zuo and G. Li, *ACS Appl. Mater. Interfaces*, 2015, **7**, 22999–23007.

11 A. Zhang, L. Zhang, G. Jing, H. Zhang, S. Wang, H. Su and S. Zeng, *Int. J. Hydrogen Energy*, 2018, **43**, 10322–10333.

12 H. Zhang, C. Xu, J. Ding, H. Su and S. Zeng, *Appl. Surf. Sci.*, 2017, **426**, 50–55.

13 J. Tan, D. Liu, X. Xu and L. Mai, *Nanoscale*, 2017, **9**, 19001–19016.

14 M. Meldal and C. W. Tornøe, *Chem. Rev.*, 2008, **108**, 2952–3015.

15 G. X. Pei, X. Y. Liu, X. Yang, L. Zhang, A. Wang, L. Li, L. H. Wang, X. Wang and T. Zhang, *ACS Catal.*, 2017, **7**, 1491–1500.

16 C. Möller, H. Fedderwitz, C. Noguera, J. Goniakowski and N. Nilius, *Phys. Chem. Chem. Phys.*, 2018, **20**, 5636–5643.

17 R.-P. Ye, L. Lin, C.-C. Chen, J.-X. Yang, F. Li, X. Zhang, D.-J. Li, Y.-Y. Qin, Z. Zhou and Y.-G. Yao, *ACS Catal.*, 2018, **8**, 3382–3394.

18 C. Tang, X. Liao, W. Zhong, H. Yu and Z. Liu, *RSC Adv.*, 2017, **7**, 6439–6446.

19 T. Usui, Z. Liu, S. Ibe, J. Zhu, C. Anand, H. Igarashi, N. Onaya, Y. Sasaki, Y. Shiramata, T. Kusamoto and T. Wakihara, *ACS Catal.*, 2018, **8**, 9165–9173.

20 K.-S. Cho, E. Kim, D.-W. Kim and H.-K. Kim, *RSC Adv.*, 2017, **7**, 45484–45494.

21 B. Cai, Y. Su, J. Hu, C. Zou and Y. Zhang, *J. Mater. Chem. C*, 2018, **6**, 1715–1721.

22 H. Kou, Y. Jiang, J. Li, S. Yu and C. Wang, *J. Mater. Chem.*, 2012, **22**, 1950–1956.

23 J. Dou, Z. Sun, A. A. Opalade, N. Wang, W. Fu and F. Tao, *Chem. Soc. Rev.*, 2017, **46**, 2001–2027.

24 M. Behrens, F. Studt, I. Kasatkin, S. Kühl, M. Hävecker, F. Abild-Pedersen, S. Zander, F. Girgsdies, P. Kurr, B.-L. Kniep, M. Tovar, R. W. Fischer, J. K. Nørskov and R. Schlögl, *Science*, 2012, **336**, 893–897.

25 X.-m. Zhang, P. Tian, W. Tu, Z. Zhang, J. Xu and Y.-F. Han, *ACS Catal.*, 2018, **8**, 5261–5275.

26 V. Petkov, Y. Maswadeh, Y. Zhao, A. Lu, H. Cronk, F. Chang, S. Shan, H. Kareem, J. Luo, C. J. Zhong, S. Shastri and P. Kenesei, *Nano Energy*, 2018, **49**, 209–220.

27 Y. Hong, S. Zhang, F. F. Tao and Y. Wang, *ACS Catal.*, 2017, **7**, 3639–3643.

28 J. Wu, H. Shan, W. Chen, X. Gu, P. Tao, C. Song, W. Shang and T. Deng, *Adv. Mater.*, 2016, **28**, 9686–9712.

29 J. P. Vivek, N. G. Berry, J. Zou, R. J. Nichols and L. J. Hardwick, *J. Phys. Chem. C*, 2017, **121**, 19657–19667.

30 S. Alayoglu, J. M. Krier, W. D. Michalak, Z. Zhu, E. Gross and G. A. Somorjai, *ACS Catal.*, 2012, **2**, 2250–2258.

31 S. Sun, X. Zhang, Q. Yang, S. Liang, X. Zhang and Z. Yang, *Prog. Mater. Sci.*, 2018, **96**, 111–173.

32 M. B. Gawande, A. Goswami, F. X. Felpin, T. Asefa, X. Huang, R. Silva, X. Zou, R. Zboril and R. S. Varma, *Chem. Rev.*, 2016, **116**, 3722–3811.

33 W. W. Wang, W. Z. Yu, P. P. Du, H. Xu, Z. Jin, R. Si, C. Ma, S. Shi, C. J. Jia and C. H. Yan, *ACS Catal.*, 2017, **7**, 1313–1329.

34 C. Paolucci, I. Khurana, A. A. Parekh, S. Li, A. J. Shih, H. Li, J. R. Di Iorio, J. D. Albarracin-Caballero, A. Yezerets, J. T. Miller, W. N. Delgass, W. N. Ribeiro, F. H. Schneider and R. Gounder, *Science*, 2017, **357**, 898–903.

35 D.-H. Nam, O. S. Bushuyev, J. Li, P. De Luna, A. Seifitokaldani, C.-T. Dinh, F. P. García de Arquer, Y. Wang, Z. Liang, A. H. Proppe, C. S. Tan, P. Todorović, O. Shekhah, C. M. Gabardo, J. W. Jo, J. Choi, M. J. Choi, S.-W. Baek, J. Kim, D. Sinton, S. O. Kelley, M. Eddaoudi and E. H. Sargent, *J. Am. Chem. Soc.*, 2018, **140**, 11378–11386.

36 B. Coşkuner Filiz, A. Kantürk Figen and S. Pişkin, *Appl. Catal., B*, 2018, **238**, 365–380.

37 Y. Zhou, F. Che, M. Liu, C. Zou, Z. Liang, P. De Luna, H. Yuan, J. Li, Z. Wang, H. Xie, H. Li, P. Chen, E. Bladt, R. Quintero-Bermudez, T.-K. Sham, S. Bals, J. Hofkens, D. Sinton, G. Chen and E. H. Sargent, *Nat. Chem.*, 2018, **10**, 974–980.

38 Y. Wang, Z. Chen, P. Han, Y. Du, Z. Gu, X. Xu and G. Zheng, *ACS Catal.*, 2018, **8**, 7113–7119.

39 W. Zhu, L. Zhang, P. Yang, C. Hu, H. Dong, Z.-J. Zhao, R. Mu and J. Gong, *ACS Energy Lett.*, 2018, **3**, 2144–2149.

40 T. Kottakkat, K. Klingan, S. Jiang, Z. P. Jovanov, V. H. Davies, G. A. M. El-Nagar, H. Dau and C. Roth, *ACS Appl. Mater. Interfaces*, 2019, **11**, 14734–14744.

41 S. Sarfraz, A. T. Garcia-Esparza, A. Jedidi, L. Cavallo and K. Takanabe, *ACS Catal.*, 2016, **6**, 2842–2851.

42 J. P. Simonovis, A. Hunt, R. M. Palomino, S. D. Senanayake and I. Waluyo, *J. Phys. Chem. C*, 2018, **122**, 4488–4495.

43 A. C. Schilling, K. Groden, J. P. Simonovis, A. Hunt, R. T. Hannagan, V. Çınar, J.-S. McEwen, E. C. H. Sykes and I. Waluyo, *ACS Catal.*, 2020, **10**, 4215–4226.

44 T. Ryu, H. Kim and S. B. Hong, *Appl. Catal., B*, 2019, **245**, 513–521.

45 W.-W. Wang, P.-P. Du, S.-H. Zou, H.-Y. He, R.-X. Wang, Z. Jin, S. Shi, Y.-Y. Huang, R. Si, Q.-S. Song, C.-J. Jia and C.-H. Yan, *ACS Catal.*, 2015, **5**, 2088–2099.

46 Y. Inomata, K. Albrecht and K. Yamamoto, *ACS Catal.*, 2018, **8**, 451–456.

47 A. Gloystein and N. Nilius, *J. Phys. Chem. C*, 2019, **123**, 26939–26946.

48 C. Wang, M. Cao, X. Jiang, M. Wang and Y. Shen, *Electrochim. Acta*, 2018, **271**, 544–550.

49 D. Ren, B. S.-H. Ang and B. S. Yeo, *ACS Catal.*, 2016, **6**, 8239–8247.

50 H. Hu, Y. Tang, Q. Hu, P. Wan, L. Dai and X. J. Yang, *Appl. Surf. Sci.*, 2018, **445**, 281–286.

51 J. H. Sinfelt, *Acc. Chem. Res.*, 1977, **10**, 15–20.

52 J. Yin, S. Shan, L. Yang, D. Mott, O. Malis, V. Petkov, F. Cai, M. Shan Ng, J. Luo, B. H. Chen, M. Engelhard and C. J. Zhong, *Chem. Mater.*, 2012, **24**, 4662–4674.

53 E. L. Clark, C. Hahn, T. F. Jaramillo and A. T. Bell, *J. Am. Chem. Soc.*, 2017, **139**, 15848–15857.

54 T. T. H. Hoang, S. Verma, S. Ma, T. T. Fister, J. Timoshenko, A. I. Frenkel, P. J. A. Kenis and A. A. Gewirth, *J. Am. Chem. Soc.*, 2018, **140**, 5791–5797.

55 B. Huang, H. Kobayashi, T. Yamamoto, S. Matsumura, Y. Nishida, K. Sato, K. Nagaoka, S. Kawaguchi, Y. Kubota and H. Kitagawa, *J. Am. Chem. Soc.*, 2017, **139**, 4643–4646.

56 Y. Liao, G. Yu, Y. Zhang, T. Guo, F. Chang and C. J. Zhong, *J. Phys. Chem. C*, 2016, **120**, 10476–10484.

57 J. Jiao, R. Lin, S. Liu, W.-C. Cheong, C. Zhang, Z. Chen, Y. Pan, J. Tang, K. Wu, S.-F. Hung, H. M. Chen, L. Zheng, Q. Lu, X. Yang, B. Xu, H. Xiao, J. Li, D. Wang, Q. Peng, C. Chen and Y. Li, *Nat. Chem.*, 2019, **11**, 222–228.

58 A. A. Peterson, F. Abild-Pedersen, F. Studt, J. Rossmeisl and J. K. Nørskov, *Energy Environ. Sci.*, 2010, **3**, 1311–1315.

59 W. J. Durand, A. A. Peterson, F. Studt, F. Abild-Pedersen and J. K. Nørskov, *Surf. Sci.*, 2011, **605**, 1354–1359.

60 L. Cao, D. Raciti, C. Li, K. J. T. Livi, P. F. Rottmann, K. J. Hemker, T. Mueller and C. Wang, *ACS Catal.*, 2017, **7**, 8578–8587.

61 Z. Wang, G. Yang, Z. Zhang, M. Jin and Y. Yin, *ACS Nano*, 2016, **10**, 4559–4564.

62 E. V. Shelepova, L. Y. Ilina and A. A. Vedyagin, *Catal. Today*, 2019, **331**, 35–42.

63 H. Song, M. Im, J. T. Song, J.-A. Lim, B.-S. Kim, Y. Kwon, S. Ryu and J. Oh, *Appl. Catal., B*, 2018, **232**, 391–396.

64 M. Tada, R. Bal, S. Namba and Y. Iwasawa, *Appl. Catal., A*, 2006, **307**, 78–84.

65 S. Shan, V. Petkov, B. Prasai, J. Wu, P. Joseph, Z. Skeete, E. Kim, D. Mott, O. Malis, J. Luo and C. J. Zhong, *Nanoscale*, 2015, **7**, 18936–18948.

66 K. Liu, M. Ma, L. Wu, M. Valenti, D. Cardenas-Morcoso, J. P. Hofmann, J. Bisquert, S. Gimenez and W. A. Smith, *ACS Appl. Mater. Interfaces*, 2019, **11**, 16546–16555.

67 M. Bernal, A. Bagger, F. Scholten, I. Sinev, A. Bergmann, M. Ahmadi, J. Rossmeisl and B. R. Cuenya, *Nano Energy*, 2018, **53**, 27–36.

68 A. Lassoued, J. Deson, C. Lalo, A. Gédéon, P. Batamack, J. Fraissard, R. Bîrjega, R. Ganea and C. Nenu, *Microporous Mesoporous Mater.*, 2001, **43**, 1–9.

69 J. Su, Z. Zhang, D. Fu, D. Liu, X.-C. Xu, B. Shi, X. Wang, R. Si, Z. Jiang, J. Xu and Y.-F. Han, *J. Catal.*, 2016, **336**, 94–106.

70 Z.-P. Wu, S. Shan, Z.-H. Xie, N. Kang, K. Park, E. Hopkins, S. Yan, A. Sharma, J. Luo, J. Wang, V. Petkov, L. Wang and C. J. Zhong, *ACS Catal.*, 2018, **8**, 11302–11313.

71 W. Zhan, J. Wang, H. Wang, J. Zhang, X. Liu, P. Zhang, M. Chi, Y. Guo, Y. Guo, G. Lu, S. Sun, S. Dai and H. Zhu, *J. Am. Chem. Soc.*, 2017, **139**, 8846–8854.

72 D. Kim, C. Xie, N. Becknell, Y. Yu, M. Karamad, K. Chan, E. J. Crumlin, J. K. Nørskov and P. Yang, *J. Am. Chem. Soc.*, 2017, **139**, 8329–8336.

73 X. Gong, H. Noh, N. C. Gianneschi and O. K. Farha, *J. Am. Chem. Soc.*, 2019, **141**, 6146–6151.

74 H. Xie, T. Wang, J. Liang, Q. Li and S. Sun, *Nano Today*, 2018, **21**, 41–54.

75 H. M. Lee, L. Juan, F. Yeh, H. Li, H. Chen, M. B. Chang, S. Chen and C. Tzeng, *IEEE Trans. Plasma Sci.*, 2009, **37**, 2213–2220.

76 Y. Wang, J. Liu, Y. Wang, A. M. Al-Enizi and G. Zheng, *Small*, 2017, **13**, 1701809.

77 D. Mellmann, P. Sponholz, H. Junge and M. Beller, *Chem. Soc. Rev.*, 2016, **45**, 3954–3988.

78 K. Mori, S. Masuda, H. Tanaka, K. Yoshizawa, M. Che and H. Yamashita, *Chem. Commun.*, 2017, **53**, 4677–4680.

79 H. Yang, C. Zhang, P. Gao, H. Wang, X. Li, L. Zhong, W. Wei and Y. Sun, *Catal. Sci. Technol.*, 2017, **7**, 4580–4598.

80 J.-H. Kim, H. Woo, S.-W. Yun, H.-W. Jung, S. Back, Y. Jung and Y.-T. Kim, *Appl. Catal., B*, 2017, **213**, 211–215.

81 Z. B. Hoffman, T. S. Gray, K. B. Moraveck, T. B. Gunnoe and G. Zangari, *ACS Catal.*, 2017, **7**, 5381–5390.

82 W. Luo, W. Xie, R. Mutschler, E. Oveisi, G. L. De Gregorio, R. Buonsanti and A. Züttel, *ACS Catal.*, 2018, **8**, 6571–6581.

83 W. Zhang, S. Shan, J. Luo, A. Fisher, J.-F. Chen, C. J. Zhong, J. Zhu and D. Cheng, *J. Phys. Chem. C*, 2017, **121**, 11010–11020.

84 D. R. Kauffman, D. R. Alfonso, D. N. Tafen, C. Wang, Y. Zhou, Y. Yu, J. W. Lekse, X. Deng, V. Espinoza, J. Trindell, O. K. Ranasingha, A. Roy, J.-S. Lee and H. L. Xin, *J. Phys. Chem. C*, 2018, **122**, 27991–28000.

85 A. Aljabour, D. H. Apaydin, H. Coskun, F. Ozel, M. Ersoz, P. Stadler, N. S. Sariciftci and M. Kus, *ACS Appl. Mater. Interfaces*, 2016, **8**, 31695–31701.

86 G. O. Barasa, T. S. Yu, X. L. Lu, X. J. Zhou, H. L. Wang, L. H. Qian, Y. Yu, L. Liu and P. X. Lei, *Electrochim. Acta*, 2019, **295**, 584–590.

87 R. Imani, Z. Qiu, R. Younesi, M. Pazoki, D. L. A. Fernandes, P. D. Mitev, T. Edvinsson and H. Tian, *Nano Energy*, 2018, **49**, 40–50.

88 S. Rasul, D. H. Anjum, A. Jedidi, Y. Minenkov, L. Cavallo and K. Takanabe, *Angew. Chem., Int. Ed.*, 2015, **54**, 2146–2150.

89 A. Jedidi, S. Rasul, D. Masih, L. Cavallo and K. Takanabe, *J. Mater. Chem. A*, 2015, **3**, 19085–19092.

90 Y. Mun, S. Lee, A. Cho, S. Kim, J. W. Han and J. Lee, *Appl. Catal., B*, 2019, **246**, 82–88.

91 S. Ma, M. Sadakiyo, M. Heima, R. Luo, R. T. Haasch, J. I. Gold, M. Yamauchi and P. J. A. Kenis, *J. Am. Chem. Soc.*, 2017, **139**, 47–50.

92 X. Jiang, N. Koizumi, X. Guo and C. Song, *Appl. Catal., B*, 2015, **170–171**, 173–185.

93 X. Nie, X. Jiang, H. Wang, W. Luo, M. J. Janik, Y. Chen, X. Guo and C. Song, *ACS Catal.*, 2018, **8**, 4873–4892.

94 Q. Li, J. Fu, W. Zhu, Z. Chen, B. Shen, L. Wu, Z. Xi, T. Wang, G. Lu, J.-J. Zhu and S. Sun, *J. Am. Chem. Soc.*, 2017, **139**, 4290–4293.

95 M. Schreier, F. Héroguel, L. Steier, S. Ahmad, J. S. Luterbacher, M. T. Mayer, J. Luo and M. Grätzel, *Nat. Energy*, 2017, **2**, 17087.

96 J. Wang, Y. Ji, Q. Shao, R. Yin, J. Guo, Y. Li and X. Huang, *Nano Energy*, 2019, **59**, 138–145.

97 A. Cao, J. Schumann, T. Wang, L. Zhang, J. Xiao, P. Bothra, Y. Liu, F. Abild-Pedersen and J. K. Nørskov, *ACS Catal.*, 2018, **8**(11), 10148–10155.

98 J. S. Hayward, P. J. Smith, S. A. Kondrat, M. Bowker and G. J. Hutchings, *Catal. Chem.*, 2017, **9**, 1655–1662.

99 F. Zhao, M. Gong, K. Cao, Y. Zhang, J. Li and R. Chen, *ChemCatChem*, 2017, **9**, 3772–3778.

100 Z. Weng, J. Jiang, Y. Wu, Z. Wu, X. Guo, K. L. Materna, W. Liu, V. S. Batista, G. W. Brudvig and H. Wang, *J. Am. Chem. Soc.*, 2016, **138**, 8076–8079.

101 D. Yang, Q. Zhu, C. Chen, H. Liu, Z. Liu, Z. Zhao, X. Zhang, S. Liu and B. Han, *Nat. Commun.*, 2019, **10**, 677.

102 L. Lu, X. Sun, J. Ma, D. Yang, H. Wu, B. Zhang, J. Zhang and B. Han, *Angew. Chem., Int. Ed.*, 2018, **57**, 14149–14153.

103 Z. Zhao and G. Lu, *J. Phys. Chem. C*, 2019, **123**, 4380–4387.

104 J. Liu, F. R. Lucci, M. Yang, S. Lee, M. D. Marcinkowski, A. J. Therrien, C. T. Williams, E. C. H. Sykes and M. Flytzani-Stephanopoulos, *J. Am. Chem. Soc.*, 2016, **138**, 6396–6399.

105 M. D. Marcinkowski, M. T. Darby, J. Liu, J. M. Wimble, F. R. Lucci, S. Lee, A. Michaelides, M. Flytzani-Stephanopoulos, M. Stamatakis and E. C. H. Sykes, *Nat. Chem.*, 2018, **10**, 325–332.

106 B. Eren, D. Torres, O. Karslıoğlu, Z. Liu, C. H. Wu, D. Stacchiola, H. Bluhm, G. A. Somorjai and M. Salmeron, *J. Am. Chem. Soc.*, 2018, **140**, 6575–6581.

107 Q. Liu, Y. Ning, W. Huang, Q. Fu, F. Yang and X. Bao, *J. Phys. Chem. C*, 2018, **122**, 8364–8372.

108 A. E. Baber, F. Xu, F. Dvorak, K. Mudiyanselage, M. Soldemo, J. Weissenrieder, S. D. Senanayake, J. T. Sadowski, J. A. Rodriguez, V. Matolín, M. G. White and D. J. Stacchiola, *J. Am. Chem. Soc.*, 2013, **135**, 16781–16784.

109 M. B. Boucher, M. D. Marcinkowski, M. L. Liriano, C. J. Murphy, E. A. Lewis, A. D. Jewell, M. F. G. Mattera, G. Kyriakou, M. Flytzani-Stephanopoulos and E. C. H. Sykes, *ACS Nano*, 2013, **7**, 6181–6187.

110 L. Luo, S. Chen, Q. Xu, Y. He, Z. Dong, L. Zhang, J. Zhu, Y. Du, B. Yang and C. Wang, *J. Am. Chem. Soc.*, 2020, **142**, 4022–4027.

111 Y. Lum and J. W. Ager, *Nat. Catal.*, 2019, **2**, 86–93.

112 F. Li, L. Chen, M. Xue, T. Williams, Y. Zhang, D. R. MacFarlane and J. Zhang, *Nano Energy*, 2017, **31**, 270–277.

113 B. Zhang, Z. Guo, Z. Zuo, W. Pan and J. Zhang, *Appl. Catal., B*, 2018, **239**, 441–449.

114 X.-M. Liu, G. Q. Lu, Z.-F. Yan and J. Beltramini, *Ind. Eng. Chem. Res.*, 2003, **42**, 6518–6530.

115 J. Wu, S. Shan, V. Petkov, B. Prasai, H. Cronk, P. Joseph, J. Luo and C. J. Zhong, *ACS Catal.*, 2015, **5**, 5317–5327.

116 V. Mukundan, S. Shan, C. J. Zhong and O. Malis, *J. Nanomater.*, 2018, **2018**, 9087320.

117 V. Mukundan, J. Yin, P. Joseph, J. Luo, S. Shan, D. N. Zakharov, C. J. Zhong and O. Malis, *Sci. Technol. Adv. Mater.*, 2014, **15**, 025002.

118 L. Ma, X. Luo, A. J. Kropf, J. Wen, X. Wang, S. Lee, D. J. Myers, D. Miller, T. Wu, J. Lu and K. Amine, *Nano Lett.*, 2016, **16**, 781–785.

119 Y. Maswadeh, S. Shan, B. Prasai, Y. Zhao, Z.-H. Xie, Z. Wu, J. Luo, Y. Ren, C. J. Zhong and V. Petkov, *J. Mater. Chem. A*, 2017, **5**, 7355–7365.

120 J. Wu, S. Shan, J. Luo, P. Joseph, V. Petkov and C. J. Zhong, *ACS Appl. Mater. Interfaces*, 2015, **7**, 25906–25913.

121 V. Petkov, S. Shastri, S. Shan, P. Joseph, J. Luo, C. J. Zhong, T. Nakamura, Y. Herbani and S. Sato, *J. Phys. Chem. C*, 2013, **117**, 22131–22141.

122 J. Yin, P. Hu, B. Wanjala, O. Malis and C. J. Zhong, *Chem. Commun.*, 2011, **47**, 9885–9887.

123 N. Kang, M. S. Ng, S. Shan, J. Wu, W. Zhao, J. Yin, W. Fang, J. Luo, V. Petkov and C. J. Zhong, *J. Power Sources*, 2016, **326**, 60–69.

124 S. Lee, G. Park and J. Lee, *ACS Catal.*, 2017, **7**, 8594–8604.

125 J. Wang, Z. Li, C. Dong, Y. Feng, J. Yang, H. Liu and X. Du, *ACS Appl. Mater. Interfaces*, 2019, **11**, 2763–2767.

126 J. Huang, M. Mensi, E. Oveisi, V. Mantella and R. Buonsanti, *J. Am. Chem. Soc.*, 2019, **141**, 2490–2499.

127 S. Yao, X. Zhang, W. Zhou, R. Gao, W. Xu, Y. Ye, L. Lin, X. Wen, P. Liu, B. Chen, E. Crumlin, J. Guo, Z. Zuo, W. Li, J. Xie, L. Lu, C. J. Kiely, L. Gu, C. Shi, J. A. Rodriguez and D. Ma, *Science*, 2017, **357**, 389.

128 J. A. Rodriguez, J. Graciani, J. Evans, J. B. Park, F. Yang, D. Stacchiola, S. D. Senanayake, S. Ma, M. Pérez, P. Liu, J. F. Sanz and J. Hrbek, *Angew. Chem., Int. Ed.*, 2009, **48**, 8047–8050.

129 K. A. Goulas, S. Sreekumar, Y. Song, P. Kharidehal, G. Gunbas, P. J. Dietrich, G. R. Johnson, Y. C. Wang, A. M. Grippo, L. C. Grabow, A. A. Gokhale and F. D. Toste, *J. Am. Chem. Soc.*, 2016, **138**, 6805–6812.

130 F. Xing, J. Jeon, T. Toyao, K. I. Shimizu and S. Furukawa, *Chem. Sci.*, 2019, **10**, 8292–8298.

131 J. Shan, F. R. Lucci, J. Liu, M. El-Soda, M. D. Marcinkowski, L. F. Allard, E. C. H. Sykes and M. Flytzani-Stephanopoulos, *Surf. Sci.*, 2016, **650**, 121–129.

132 Y. Li, Z. Wei, F. Gao, L. Kovarik, R. A. L. Baylon, C. H. F. Peden and Y. Wang, *ACS Catal.*, 2015, **5**, 3006–3012.

133 W. Tu and Y. H. Chin, *ACS Catal.*, 2015, **5**, 3375–3386.

134 Z.-H. Xue, J.-T. Han, W.-J. Feng, Q.-Y. Yu, X.-H. Li, M. Antonietti and J.-S. Chen, *Angew. Chem., Int. Ed.*, 2018, **57**, 2697–2701.

135 S. M. Johnston, A. Mulligan, V. Dhanak and M. Kadodwala, *Surf. Sci.*, 2003, **530**, 111–119.

136 Q. Liu, L. Wu, S. Gülak, N. Rockstroh, R. Jackstell and M. Beller, *Angew. Chem., Int. Ed.*, 2014, **53**, 7085–7088.

137 J. Florek-Milewska, P. Decyk and M. Ziolek, *Appl. Catal., A*, 2011, **393**, 215–224.

138 E. A. Bielinski, M. Förster, Y. Zhang, W. H. Bernskoetter, N. Hazari and M. C. Holthausen, *ACS Catal.*, 2015, **5**, 2404–2415.

139 L. Zou, P. Cao, Y. Lei, D. Zakharov, X. Sun, S. House, L. Luo, J. Li, Y. Yang, Q. Yin, X. Chen, C. Li, H. Qin, E. A. Stach, J. C. Yang, G. Wang and G. W. Zhou, *Nat. Commun.*, 2020, **11**, 3934.

140 C. Li, Q. Liu, J. A. Boscoboinik and G. Zhou, Tuning the surface composition of Cu3Au binary alloy, *Phys. Chem. Chem. Phys.*, 2020, **22**, 3379–3389.

141 Z. P. Wu, D. T. Caracciolo, Y. Maswadeh, J. Wen, Z. Kong, S. Shan, J. A. Vargas, S. Yan, E. Hopkins, K. Park, A. Sharma, Y. Ren, V. Petkov, L. Wang and C. J. Zhong, *Nat. Commun.*, 2021, **12**, 859.

142 Z. P. Wu, S. Shan, S. Q. Zang and C. J. Zhong, *Acc. Chem. Res.*, 2020, **53**, 2913–2924.

143 S. Shan, J. Li, Y. Maswadeh, C. O'Brien, H. Kareeml, D. T. Tran, I. C. Lee, Z. P. Wu, S. Wang, S. Yan, H. Cronk, D. Mott, L. Yang, J. Luo, V. Petkov and C. J. Zhong, *Nat. Commun.*, 2020, **11**, 4201.

144 T. Koitaya, S. Yamamoto, Y. Shiozawa, Y. Yoshikura, M. Hasegawa, J. Tang, K. Takeuchi, K. Mukai, S. Yoshimoto, I. Matsuda and J. Yoshinobu, *ACS Catal.*, 2019, **9**, 4539–4550.

145 S. Yan, S. Shan, J. Wen, J. Li, N. Kang, Z. Wu, J. Lombardi, H. W. Cheng, J. Wang, J. Luo, N. He, D. Mott, L. Wang, Q. Ge, B. S. Hsiao, M. Poliks and C. J. Zhong, *Adv. Mater.*, 2020, **32**, 2002171.